ENVIRONMENTAL RESEARCH LETTERS

LETTER • OPEN ACCESS

Water budget-based evapotranspiration product captures natural and human-caused variability

To cite this article: Shubham Goswami *et al* 2024 *Environ. Res. Lett.* **19** 094034

View the article online for updates and enhancements.

ENVIRONMENTAL RESEARCH
LETTERS

OPEN ACCESS

RECEIVED
30 January 2024

REVISED
23 June 2024

ACCEPTED FOR PUBLICATION
16 July 2024

PUBLISHED
16 August 2024

LETTER

Water budget-based evapotranspiration product captures natural and human-caused variability

Shubham Goswami[1,9], Chirag Rajendra Ternikar[1,9], Rajsekhar Kandala[1], Netra S Pillai[2,4], Vivek Kumar Yadav[3], Abhishek[3,5], Jisha Joseph[6], Subimal Ghosh[7,8] and Bramha Dutt Vishwakarma[2,3,*]

[1] Department of Civil Engineering, IISc, Bangalore, India
[2] Centre for Earth Science, IISc, Bangalore, India
[3] Interdisciplinary Centre for Water Research, IISc, Bangalore, India
[4] Indian Space Research Organization, Bangalore, India
[5] Department of Civil Engineering, Indian Institute of Technology Roorkee, Roorkee, India
[6] Potsdam Institute for Climate Impact Research, Potsdam, Germany
[7] Department of Civil Engineering, Indian Institute of Technology Bombay, Mumbai, India
[8] IDP Climate Studies, Indian Institute of Technology Bombay, Mumbai, India
[9] These authors contributed equally.
[*] Author to whom any correspondence should be addressed.

E-mail: bramha@iisc.ac.in

Keywords: evapotranspiration, water budget, Kalman filter, global ET product, GRACE, Ganges, spatiotemporal variability

Abstract

Evapotranspiration (*ET*) is one of the most important yet highly uncertain components of the water cycle. Available modeled *ET* products do not necessarily agree with each other at various spatiotemporal scales, either due to limitations on input data and/or due to model assumptions and simplifications. Therefore, using the water budget equation to estimate *ET* has gained attention. However, numerous water budget combinations with large uncertainties are available, which increases ambiguity in choosing the best *ET* estimate. Here, the Kalman filter is employed to ingest 96 water budget-based *ET* estimates, and produce a global *ET* product with uncertainty <2 mm month^{-1}, and capture the general spatiotemporal pattern of *ET* and the inter-annual variability over all continents. Since the water budget includes storage changes due to human interventions, our *ET* estimates are superior over regions with strong irrigation signals, such as the Ganges basin. We verify our claim by using a modified variable infiltration capacity model that also simulates irrigation activities. Our *ET* estimates have a global mean positive trend of 0.18 ± 0.02 mm yr^{-1} with larger regional variations, which we discuss.

1. Introduction

Based on several general circulation model (GCM) runs for various future climate scenarios, the IPCC AR6 states that the global water cycle will be severely affected by anthropogenic global warming (Douville *et al* 2021). Although the GCM predictions largely agree at the global-mean scale, they tend to diverge at the regional scale for all water cycle components: precipitation (P), actual evapotranspiration (ET), runoff (R) and storage change (ΔS). Therefore, capturing the predicted acceleration of water cycle components in the observed data is imperative for increasing confidence in future projections (Dorigo *et al* 2021). Among the water cycle components, P and ΔS are available with good accuracy at the catchment scale for regional analysis. However, R and ET have large uncertainties. Global ET estimates are derived from various near-surface observations, such as temperature, relative humidity, precipitation, land use and land cover, etc. These variables are themselves poorly observed, and the relation used for estimating ET has several assumptions and approximations that increase the uncertainties in ET products (Badgley *et al* 2015, Lehmann *et al* 2022, Zhu *et al* 2022). Since ET is a key component for understanding the energy-carbon-food nexus, several efforts are ongoing to improve ET estimates, ranging from improving the models and input data quality to novel ways of estimating ET. For example, assimilating remotely sensed hydro-meteorological variables in land surface models (Bhattarai *et al* 2019, Zhu *et al* 2022). Employing an ensemble Kalman filter in a two-step procedure, first, water-budget measurements are assimilated into a variable infiltration capacity (VIC) model and then the water-budget variables are optimally updated by ensuring water-budget closure (Pan and Wood 2006). Another study estimated runoff using an ensemble Kalman filter and a simple water-budget equation instead of using land surface models (Lorenz *et al* 2015). To tackle high uncertainties in global estimates of water fluxes, the Kalman filter has been used. However, the major challenge in using the Kalman filter as a predictor for *ET* estimation is setting up a state transition matrix that must accurately capture the spatiotemporal variability in *ET* due to both climatic and anthropogenic factors while using only a few available global observations.

Alternatively, the water-budget equation that relates *P* to *ET*, *R* and ΔS, can be used to estimate *ET* without modeling the anthropogenic or climatic variations explicitly because the water budget follows mass conservation (Rodell *et al* 2011, Syed *et al* 2014, Liu *et al* 2016, Baker *et al* 2021, Shao *et al* 2022). If the storage has changed, it must be attributed to other outgoing fluxes, *R* and *ET*. Therefore, several studies have used the water balance equation to validate a modeled water-budget component or to estimate them (Rodell *et al* 2004, Lorenz *et al* 2015, Liu *et al* 2016, Mao and Wang 2017, Xiong *et al* 2023). Since there are several products for each water-budget component, many combinations exist, and each would provide a different estimate for *ET* (Lorenz *et al* 2015, Liu *et al* 2016). Moreover, there is no consensus on the best available global products for closing the water budget comprehensively (Lehmann *et al* 2022). Hence, the accuracy of this approach is subject to the accuracy of the water-budget component products. Nevertheless, *ET* estimates from the water budget are valuable as they are an independent data set free from the propagation and/or amplification of the uncertainties in forcing data and biases from model approximations (Long *et al* 2014, Xiong *et al* 2023). With available global products of water-budget components, one can generate several thousand realizations of *ET*. An equal weight means that *ET* can be obtained from those thousands of combinations but with a large uncertainty or standard deviation (Xiong *et al* 2023). To tackle this, the Kalman filter is employed here, which is an excellent tool for solving the estimation problems in environmental sciences (Rougier *et al* 2023).

Using GRACE data into the water budget to derive *ET* estimates provides a unique opportunity to account for *ET* increases due to human-driven water storage changes, which otherwise is not possible (Rodell *et al* 2004, Lorenz *et al* 2015, Vishwakarma 2020). The use of the Kalman filter will help in converging to the near-true estimate of *ET* (Lorenz *et al* 2015, Rougier *et al* 2023). Here, 96 *ET* estimates, from water-budget combinations where uncertainties are available, for a point in time at 1° grid resolution are used as observations in a Kalman filter initialized with ERA5 *ET* estimate as the first guess. *ET* from the Kalman filter stabilizes after ingesting around 30 combinations in random order, and has an uncertainty <2 mm month^{-1}, which is significantly smaller than the 1σ spread of *ET* from thousands of combinations or a weighted average of those 30 combinations. Our approach is resilient to various issues, such as outliers, the influence of any single input from the combinations, the sequence of data ingestions, inflated uncertainties, and initial value assumptions. Details on the method and data are provided in the dedicated sections below. The Kalman filter ET(referred to as KF-ET) is significantly different from the initial guess (ERA5) with a larger range and a better representation of climate-driven inter-annual and human-driven intra-annual variability. Over the Ganges river basin, a modified VIC model was used to demonstrate that the difference between KF-ET and ERA5 *ET* originates from irrigation activities. KF-ET compares well with the *in situ* Fluxnet data for selected sites. Overall, a global mean trend of 0.18 $\pm$ 0.02 mm yr^{-1} between 2003 and 2016 is obtained from KF-ET, which is expected due to climate change as reported in the IPCC report (Douville *et al* 2021).

2. Method

The water-budget equation follows the law of conservation of mass. The input to a river catchment, i.e. precipitation (*P*), can be written as the sum of runoff (*R*), rate of storage change ($\frac{\mathrm{d}S}{\mathrm{d}t}$), and *ET*:

$$P = R + ET + \frac{\mathrm{d}S}{\mathrm{d}t}. \tag{1}$$

Closing the water budget is essential to demonstrate confidence in observations and simulations of water-budget components. With advances in remote sensing and modeling, water-budget components are available at better spatiotemporal scales. For example, remote sensing-based global precipitation products with acceptable accuracy have been available since 1979 (Huffman *et al* 2015, Rustemeier *et al* 2022). Although observed *R* is available only for a few gauged catchments (GRDC 2020), there are several model outputs, such as those from land surface models (LSMs) or global hydrological models or machine learning-based products like GRUN that have been shown to capture the runoff very well (Ghiggi *et al* 2019, 2021). Rate of storage change ($\frac{\mathrm{d}S}{\mathrm{d}t}$) has been available at unprecedented accuracy from the Gravity Recovery and Climate Experiment (GRACE) satellite mission since 2002 (Watkins *et al* 2015, Vishwakarma 2020). However, there are no direct *ET* estimates at the global scale and they are conventionally derived using observations of various surface properties and hydrometeorological variables. There are several methods for estimating *ET* with inherent assumptions and approximations, resulting in high uncertainties in ET products (Badgley *et al* 2015, Fisher *et al* 2017). As a result, several studies in the past decade have tried to estimate ET using equation (1) with the most appropriate P, R and S available (Pan *et al* 2008, Rodell *et al* 2011, Syed *et al* 2014, Bhattarai *et al* 2019). There are a number of global P and R products leading to several thousand ET estimates over a location. For example, Lehmann *et al* (2022) generated approximately 1700 combinations in an attempt to close the global water budget, and Xiong *et al* (2023) could generate 4669 combinations. Xiong *et al* (2023) provided a first-ever comprehensive water budget-based global ET product with a large spread. Recent studies have elevated water budget as a potential tool for assessing the quality of model outputs, as well as estimating water budget components. Here, the classic Kalman filter is used to ingest various combinations of water budget components and provide a robust estimate of ET.

In this study, the Kalman filter algorithm (Kalman 1960) is implemented recursively on 96 ET estimates from the water budget to provide an ET product with reduced uncertainty. Since the method requires initialization, ERA5 data are used to initialize the Kalman filter algorithm, i.e. ET_0 and UET_0. However, this is not critical and one may choose any ET data to start with (see appendices A and B). In this case, the state transition matrix is a unit matrix while the initial error covariance matrix is reduced to a diagonal matrix with each diagonal entry containing UET_0 corresponding to a grid cell. First, the Kalman gain is calculated using equation (2). Then, the ET estimate and its uncertainty are updated using equations (3) and (4), respectively. The algorithm continues until all water budget ET estimates are used, i.e. $n = 96$. The procedure is applied for each grid-cell and for each monthly time-step independently. The detailed step-by-step procedure is presented in figure 1(a) (details in appendix A and table A1),

$$KG_n = \frac{UET^u_{n-1}}{UET_n + UET^u_{n-1}}, \tag{2}$$

$$ET^u_n = ET^u_{n-1} + KG_n \left(ET_n - ET^u_{n-1}\right), \tag{3}$$

$$UET^u_n = (1 - KG_n)\, UET^u_{n-1}, \tag{4}$$

where n is the number of water budget ET estimates.

3. Data

Four openly available data sets for P, eight for R and three for S are used to generate 96 ($= 4 \times 8 \times 3$) combinations with global land coverage. Details of the data set used are given in table 1. These products were chosen because uncertainty estimation for them was straightforward; formal uncertainties were available for all except for the reanalysis data set where 1σ (standard deviation) of ensembles was taken as uncertainty. All the high-resolution data sets were resampled to a regular grid of $1^\circ \times 1^\circ$ via area-weighted averaging. As suggested, P and R are smoothed using a simple moving window average of size three (equation (5)) (Lehmann *et al* 2022). Storage change (ΔS) is evaluated from S by computing the time derivative with a centered finite difference scheme (equation (6)) (Landerer and Swenson 2012, Long *et al* 2014, Lorenz *et al* 2015, Lehmann *et al* 2022),

$$X(t) = \frac{1}{4}X(t-1) + \frac{1}{2}X(t) + \frac{1}{4}X(t+1); X = P, R, \tag{5}$$

$$\Delta S(t) = \frac{S(t+1) - S(t-1)}{2}. \tag{6}$$

The time period chosen is from January 2003–December 2016 due to the following reasons: (a) GRACE observations are reliable in this duration, (b) intermittent gaps in GRACE data are filled using cubic spline interpolation, which is not suitable for longer gaps as the one between GRACE and GRACE-FO, c) water budget computation does not use ΔS but the time derivative of ΔS, which demands continuous data. R from GRUN is available only until 2014, so the number of ET estimates is reduced to 84 from 96 during 2015–2016. For basin scale analysis, major river basins with an area larger than 65 000 km^2 are chosen to satisfy the nominal resolution of GRACE products at catchment scale (Vishwakarma *et al* 2018). The shapefiles for these catchments studied are taken from the Global Runoff Data Center (GRDC 2020).

Eddy covariance data are collected for 24 sites so that they have the same LULC class as the 1° IGBP ISLSCP_II data set (details at in the table in appendices D and E). The latent heat flux (LE) data obtained for these sites are converted to ET using a λ (latent heat of evaporation) value of 2.45 MJ Kg^{-1} (equation (7)),

$$ET = \frac{LE}{\lambda} * 3600 * 24 * 30. \tag{7}$$

The IGBP-based LULC data set, including 17 detailed classes, is aggregated into nine major classes: forests, shrublands, savannas, grasslands, wetlands, croplands, natural vegetation, snow and ice, and barren. The present climate Köppen zone data (Beck *et al* 2018) with 30 detailed zones are also aggregated into five major zones, namely tropical, arid, temperate, cold and polar. Finally, the global digital elevation data set is classified into five elevation zones (Wrzesien *et al* 2019) as follows: very low (0.1–300 m), low (301–1000 m), medium (1001–1500 m), high (1501–2500 m) and very high ($\geqslant$2501 m) elevation.

Table 1. Details of data sets used in analysis, comparison and derivation of KF-ET.

Variable	Data source	Resolution		Duration	Uncertainty	Ref.
		Spatial	Temporal			
Runoff (R)	GLDAS_NOAH	0.25°	Monthly	01-2000 –…	Assumed	(Beaudoing and Rodell 2020a)
	GLDAS_CLSM	1°	Monthly	01-2000 –…	Assumed	(Li *et al* 2020)
	GLDAS_VIC	1°	Monthly	01-2000 – …	Assumed	(Beaudoing and Rodell 2020b)
	GRUN	0.5°	Monthly	01-1902 – 12-2014	Calculated	(Ghiggi *et al* 2019)
	GRUN_CRUTS4.4	0.5°	Monthly	07-1901 – 12-2019	Calculated	(Ghiggi *et al* 2021)
	GRUN_ERA5	0.5°	Monthly	07-1981 – 12-2019	Calculated	(Ghiggi *et al* 2021)
	GRUN_MERRA2	0.5°	Monthly	07-1980 – 12-2019	Calculated	(Ghiggi *et al* 2021)
	GRUN_WFDE5_CRU	0.5°	Monthly	07-1979 – 12-2018	Calculated	(Ghiggi *et al* 2021)
Precipitation (P)	ERA5	0.25°	Monthly	01-1940 – …	Calculated	(Muñoz-Sabater *et al* 2021)
	ERA5_COBRA	1.0°	Monthly	01-2000 – 12-2017	Available	(Konrad *et al* 2022)
	GPCC	1.0°	Monthly	01-2000 – …	Available	(Rustemeier *et al* 2022)
	IMERG	0.1°	Daily	06-2000 – …	Available	(Huffman *et al* 2015)
Storage (S)	JPL_MASCONS	1°	Monthly	04-2002 –…	Available	(Watkins *et al* 2015)
	CSR_LANDMASS	1°	Monthly	04-2002 –…	Available	(Landerer and Swenson 2012)
	GFZ_LANDMASS	1°	Monthly	04-2002 –…	Available	(Landerer and Swenson 2012)
Evapotranspiration (ET)	ERA5$^+$	0.25°	Monthly	01-1940 –…	Calculated	(Hersbach *et al* 2023)
	FLUXCOM	0.5°	Monthly	01-2001 – 12-2013	—	(Jung *et al* 2019)
Latent heat of evaporation (LE)	Fluxnet	Point data	Monthly	01-2003 – 12-2016	—	(Pastorello *et al* 2020)
Land use land cover (LULC)	ISLSCP_II	1°	—	—	—	(Loveland *et al* 2009)
Climate Köppen zones	GLOH20	0.5°	—	—	—	(Beck *et al* 2018)
Digital elevation model (DEM)	ISLSCP_II	1°	—	—	—	(Verdin *et al* 2011)
El Niño southern oscillation (ENSO 3.4)	NCEP-NCAR	—	—	—	—	(Trenberth and Stepaniak 2001)

Available–uncertainty is available/provided with the data sets
Assumed–uncertainty is assumed to be 100% of the value
Calculated–uncertainty calculated as 1σ of ensemble provided

4. Comparison and validation of KF-ET

Since the Kalman filter is initialized with ET from ERA5, KF-ET is first compared with ERA5 at annual scale for the year 2003 in terms of global spatial distribution (figures 1(b) and (c)). Annual ET for 2003 from ERA5 ranged between −5.57 and 1772.83 mm (median 426 mm) while KF-ET ranges between −43.62 and 1956.06 mm (median 350 mm) covering a broader range than ERA5. The median and maximum uncertainty values of the annual ET from ERA5 are 6.91 and 47.3 mm, which are reduced to 1.32 and 4.3 mm, respectively, for KF-ET (figures 1(d) and (e)). The large-scale spatial behaviors are comparable, but the amplitudes are significantly different to ERA5. Based on the uncertainty plots in the annual ET estimates from ERA5 and KF-ET (figures 1(d) and (e)), it is evident that KF-ET can bring down the uncertainty in ET estimates by an order of magnitude. The cumulative distribution function for both data sets (figure 1(f)) shows that KF-ET covers a larger variation and captures a more contrasting spatial distribution (figure 1(g)) than ERA5. The difference between ERA5 and KF-ET (figure 1(g)) indicates the absence of any systematic bias with the initial data set (i.e. ERA5). Higher uncertainties are observed in regions with higher annual ET values and lower uncertainties for regions with lower annual ET (figures 1(b)–(e)). Both KF-ET and its associated uncertainty are positively

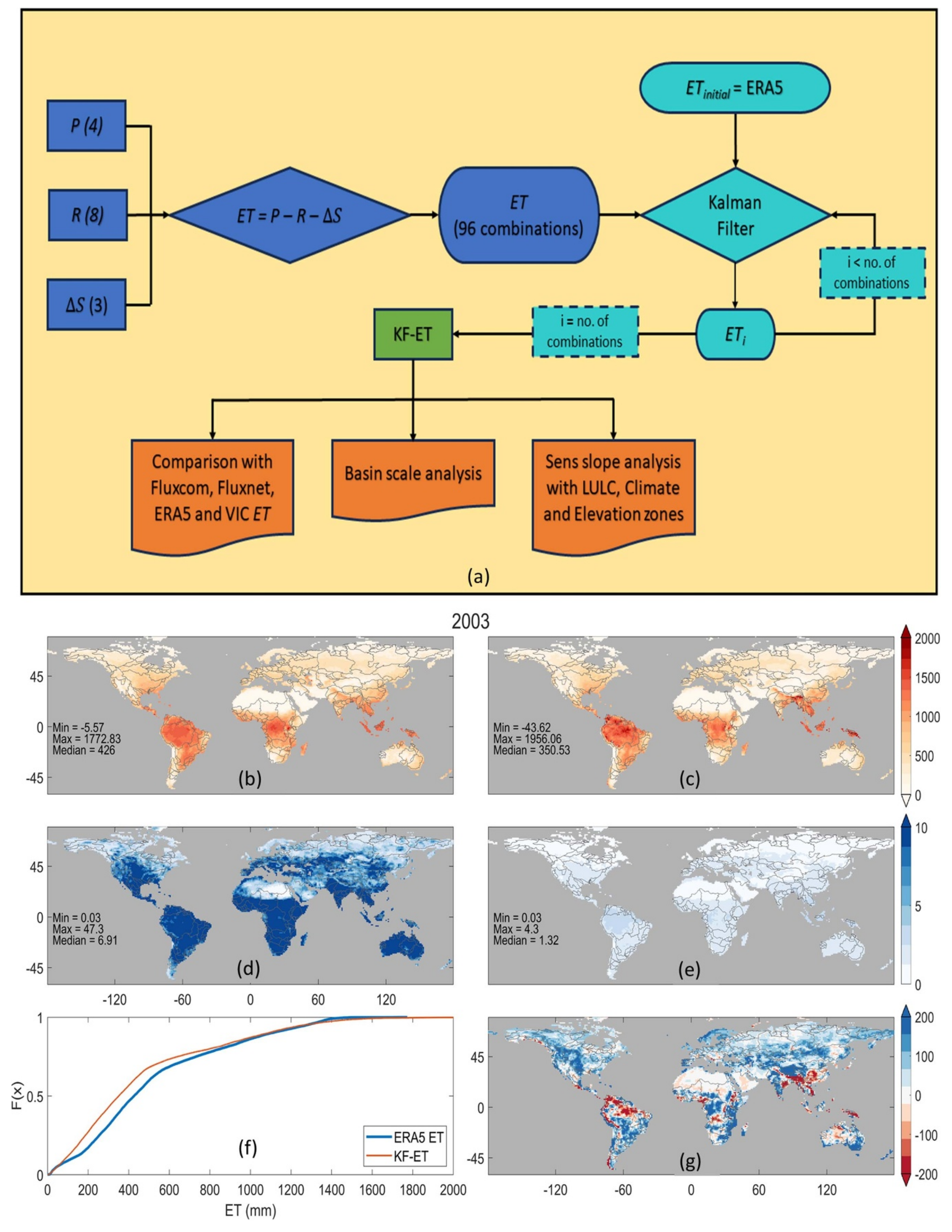

Figure 1. (a) Overview of the study with a flowchart for the methodology proposed to derive KF-ET. Comparison of annual *ET* (mm) from (b) ERA5 and (c) derived KF-ET for the year 2003 along with respective uncertainties (d) and (e). (f) CDF of annual *ET* (mm) for ERA5 and KF-ET including all land grids and (g) difference between annual *ET* from ERA5 and KF-ET.

skewed (figure A1 in appendix A). The large difference between ERA5 and KF-ET observed in the Amazon River basin, eastern India and southern China can be attributed to the presence of forests as the dominant land cover class, where ERA5 has been shown to underestimate *ET* (Baker *et al* 2021). A detailed explanation for the same is presented in sections 5.1 and 5.2 in context of the Ganges basin and the Amazon River basin, respectively.

Only 30 *ET* estimates from water budget combinations are required for the uncertainty in KF-ET to go below an acceptable threshold of < 2 mm month^{-1} (figure B1 and appendix B). While this number would vary from one month to another, it is consistently the highest for July. This result is intuitive because most of the land mass is in the Northern Hemisphere where July is the peak of summer. The order in which the combinations are fed into the framework

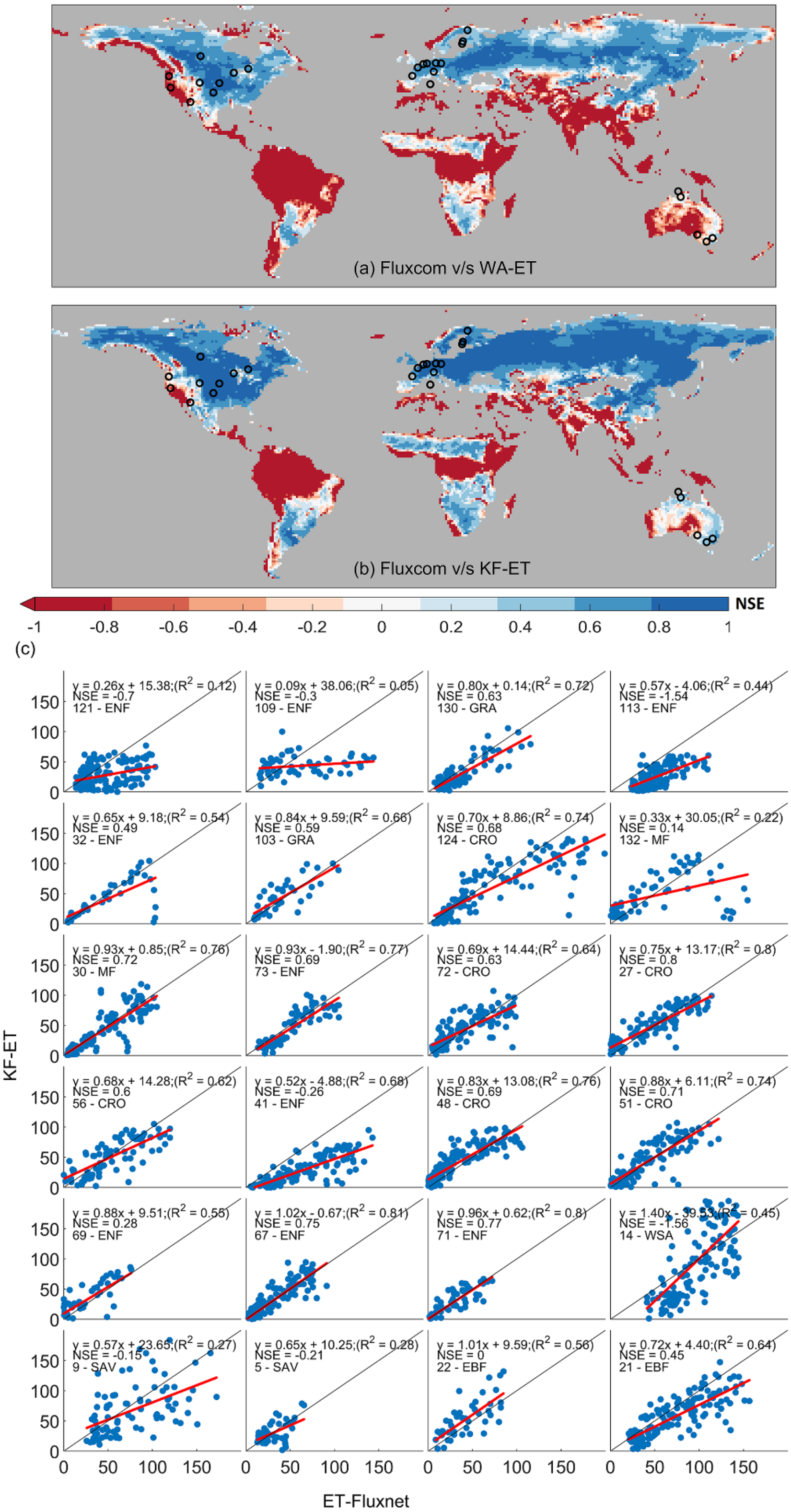

Figure 2. Comparison of Fluxcom-based *ET* with respect to (a) WA-ET and (b) KF-ET in terms of NSE and (c) scatter plots of Fluxnet-based *ET* with respect to KF-ET. Exact locations of these 24 sites (the black circle in (a) and (b)) could be related to table appendix D. Red line (best fit line), black line (1:1 line), R^2, NSE, site-id and the IGBP LULC class are reported.

and the choice of an initial guess do not affect the final output (see appendix B). To this end, it can be safely concluded that a Kalman filter-based *ET* when fed with a limited number of water budget combinations can provide stable *ET* estimates with acceptable uncertainties.

Theoretically, the weighted average of a large quantity of water budget-based *ET* should ideally be close to KF-ET. Since only a limited number of observations are available, also with large uncertainties, using the Kalman filter, a recursive method that converges to the truth, is a better choice. This is demonstrated in figures 2(a) and (b), where KF-ET and the weighted average *ET* (referred to as WA-ET hereon) are compared with the Fluxcom product. WA-ET is estimated based on the inverse variance weighting approach by Sinha *et al* (2011) (details in appendix C). Higher NSE values are observed in the Northern Hemisphere compared to the Southern Hemisphere (figures 2(a) and (b)), with NSE values for KF-ET consistently higher than WA-ET (more blue shades in the Northern Hemisphere and fewer red shades in the Southern Hemisphere).

A comparison of KF-ET with *ET* products from ERA5, GLEAM, WGHM and Fluxcom is provided in figure D1 and appendix D. Systematic improvements could be observed in parts of the USA, Africa, India, Russia and Australia when comparing KF-ET with the Fluxcom product in comparison to other *ET* products evaluated against Fluxcom. Fluxcom is not an *in situ* product and has large uncertainties in data-sparse regions. Therefore, the eddy-covariance tower data from Fluxnet is routinely used to evaluate various products, including *ET* (Zhang *et al* 2010, Miralles *et al* 2011, Mu *et al* 2011, Munier *et al* 2014, Pastorello *et al* 2020, Elnashar *et al* 2021, Tang *et al* 2024). Comparing KF-ET at 1° grid resolution with point data is challenging since *ET* is very dynamic and can change significantly within a few hundred meters. Consequently, a perfect match is not anticipated unless atmospheric conditions are exceptionally calm and land-surface cover is homogeneous. The choice of Fluxnet sites is detailed in appendix E. Despite the differences in scales (appendix E), an overall good agreement is observed for most sites (figure 2(c)); 15 out of 24 sites exhibit a positive NSE.

Direct validation of global *ET* products is challenging (Pastorello *et al* 2020, Elnashar *et al* 2021) and it remains so for this study as well. Alternatively, capturing climate- and human-driven intra-annual water-cycle variations in basins with known characteristics can serve as inference-based validation. In figures 3(a) and (b), the area-weighted average of KF-ET is shown for major river basins worldwide. The strongest variability is obtained over the Amazon, and the weakest is over the Lena River basin. The observed inter-annual variability over the Ganges is particularly interesting. North India was going through a multi-year dry phase between 2007 and 2010, and then 2010–2011 was one of the strongest La Niña events (figure 3(c)). During the dry period, precipitation declined, and then there was positively anomalous water in 2011. In a natural catchment, less precipitation would result in less *ET* due to limited water availability on the surface. However, the Ganges has a strong anthropogenic component (Joseph *et al* 2022, Joseph and Ghosh 2023). In the dry period, irrigation leads to positively anomalous *ET*. When more water is available, such as in 2011, then higher *ET* is expected (Seneviratne *et al* 2010, Greve *et al* 2014). This is better captured by KF-ET than ERA5 (figure 3(c)). These inferences are supported through case-specific modeling that is discussed next.

5. Discussion and interpretation of KF-ET

ET in a natural catchment can be estimated by variables, such as incoming radiation, soil moisture, ground heat flux, vapor pressure deficit, atmospheric conductance, canopy conductance, etc (Penman 1948), Allen and Pruitt 1986, Jensen *et al* 1990, Allen *et al* 1998). However, in catchments with significant anthropogenic action, such as irrigation, estimating *ET* becomes a challenging task. Flood irrigation is a common practice in several Southeast Asian countries, including India, where standing still water levels of about 30 cm are maintained in the field to support the growth of paddy saplings (Wei *et al* 2023).

5.1. The Ganges

Agriculture is the dominant activity in the Ganges River basin, with rice in paddies being the most preferred crop (Joseph *et al* 2022). The government subsidized electricity to support flood irrigation that begins in June, when saplings are typically transplanted (Joseph and Ghosh 2023). Hence, the surface characteristics change very rapidly from dry and bare soil in May to flooded fields with minimal vegetation in June and finally to flooded fields with significant vegetation in July and August. ERA5 and other global *ET* products ignore flooding and use vegetation growth indicators such as NDVI and LAI for *ET* estimation, which are negligible in June (Joseph and Ghosh 2023). Furthermore, eddy-covariance measurements in the Ganges (flux tower data from Kanpur, India) between 2016 and 2017 (figure F1) show that the net radiation is higher (relative humidity is lower) in June than in July and August (Morrison *et al* 2019). Taking all these factors into account, *ET* is expected to peak in June, as captured by KF-ET, while ERA5 estimates a peak in July and August.

To validate this hypothesis, a modified VIC model by Joseph and Ghosh (2023) was employed to mimic irrigation practices in the Ganges by incorporating crop-specific water usage data from past field studies (more details in Joseph *et al* (2022), Joseph and Ghosh (2023)). The model adjusts the water and energy balance processes to accommodate ponded paddy fields by proper parameterization to provide daily *ET* estimates. The *ET* values obtained were time averaged to match the temporal resolution of KF-ET (figures 3(c) and F2 in appendix F). Similar temporal patterns can be observed between KF-ET and VIC-IRR-Intermittent (figure 3(c)). A systematic bias of 25 mm was observed between the KF-ET and time-averaged VIC-IRR-Intermittent,

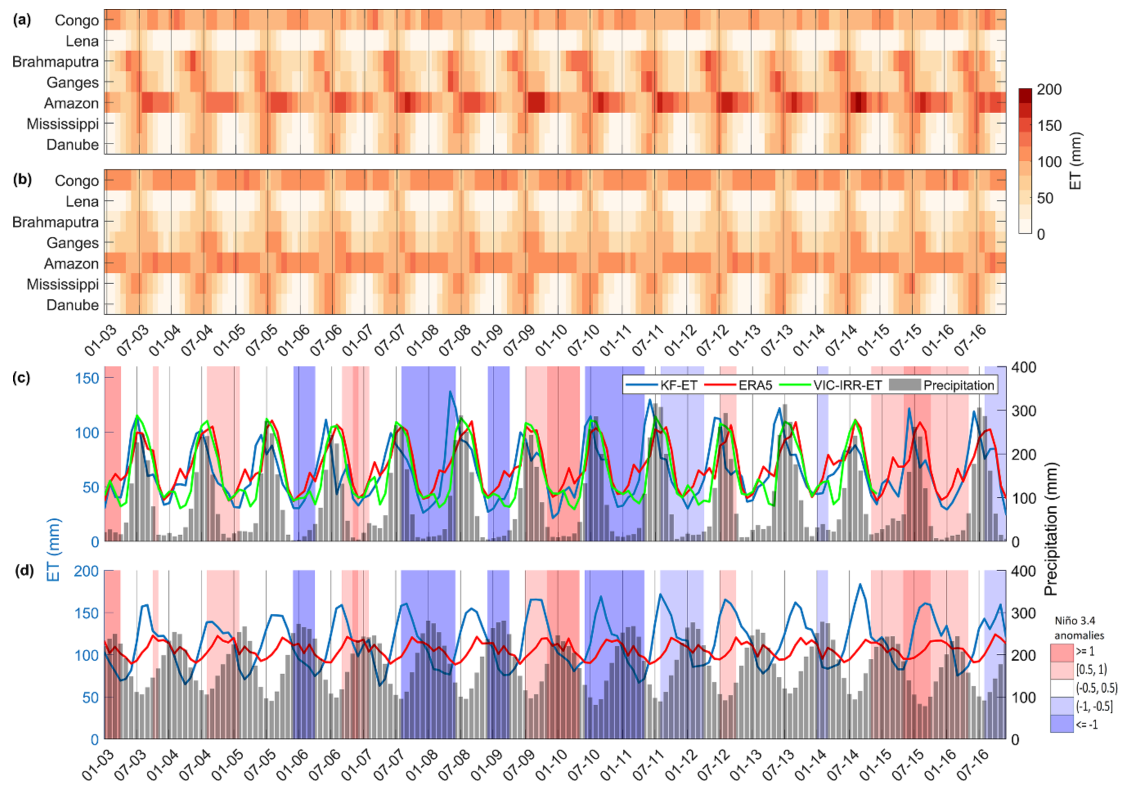

Figure 3. Basin-averaged *ET* (mm/month) time-series estimated using (a) KF-ET and (b) ERA5. Further comparison of both products over (c) the Ganges and (d) Amazon basin overlaid with ENSO 3.4 anomaly and precipitation.

which originates from assuming negligible evaporation from open water areas in the Ganges basin (∼5% of the total area).

5.2. The Amazon

Over the Amazon River basin, the inter-annual variability and seasonality are better captured by KF-ET in comparison to ERA5 (figure 3(d)). The KF-ET estimates increase from June to September (wet season) and then decrease from December to March (dry season), as consistently demonstrated in many studies utilizing flux tower data and water budget models (Saleska *et al* 2003, Wu *et al* 2016, Swann and Koven 2017, Paca *et al* 2019, Baker *et al* 2021). However, ERA5 *ET* has a smaller amplitude and follows the same seasonal cycle as precipitation, peaking during the wettest part of the year (Werth and Avissar 2004, Baker *et al* 2021). ERA5's limitations in capturing the magnitude and phase of *ET* can be attributed to the absence of accurate localized precipitation intensities, inadequate representation of *ET* feedback mechanisms, and deficiencies in accounting for deep root processes (Medvigy *et al* 2010, Verbeeck *et al* 2011, Swann and Koven 2017, Baker *et al* 2021), as extensively discussed in Swann and Koven (2017) and Baker *et al* (2021). *ET* values over the Amazon are primarily driven by energy in areas with abundant precipitation and water availability, with vegetation response as a secondary limiting factor (Gentine *et al* 2012, Swann and Koven 2017, Baker *et al* 2021). The net radiation is higher and humidity is lower during the dry season in the Amazon River basin, and the *ET* is expected to be in-phase with the net radiation cycle (Costa *et al* 2004, von Randow *et al* 2004, Werth and Avissar 2004, Hasler and Avissar 2007, O'Connor *et al* 2019). Increased *ET* before the end of the dry season is explained by access to deeper soil water by the forest, making the process energy limited and unaffected by precipitation (Seneviratne *et al* 2010, Maeda *et al* 2017). In particular, in regions with high precipitation, ERA5 struggles to accurately depict *ET* peaks due to discrepancies in precipitation inputs and deep root representation (Baker *et al* 2021). The *ET* values during the wet season are overestimated by ERA5, possibly due to the absence of a localized *ET* feedback mechanism. A localized *ET* feedback mechanism would better represent cloudy conditions that restrict energy availability, thus generating lower *ET* values (Swann and Koven 2017).

5.3. Global trends in *ET*

The assessment of global annual *ET* trends in the literature suggests contrasting studies both for seemingly intuitive reasons. A set of studies suggests an increase in the annual *ET* trend (1.1–2.2 mm yr^{-1}) from 1982–1998 and no significant trend after 1998 till 2009 (Zeng *et al* 2012, 2014). Similar increasing trends were reported by Zhang *et al* (2016) (0.54 mm yr^{-1} between 1981 and 2012) and Pan *et al* (2020) (0.0–0.62 mm yr^{-1} between 1982 and

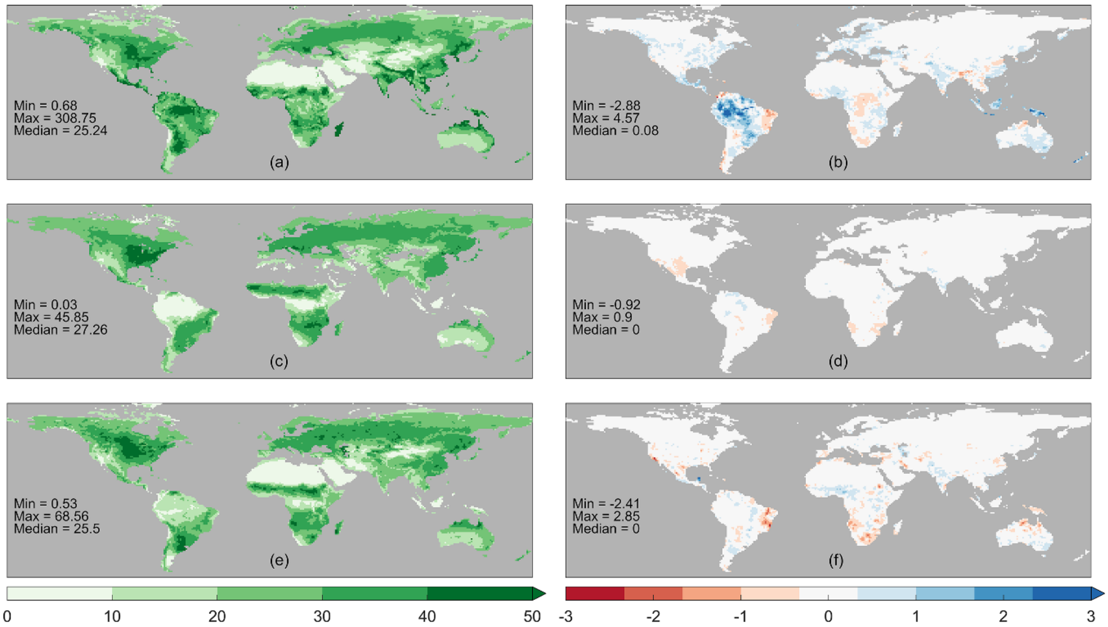

Figure 4. Standard deviation in *ET* time-series and the corresponding Sen's slope (mm/year), respectively, for (a), (b) KF-ET; (c), (d) Fluxcom; and (e), (f) ERA5.

2011). In contrast, simulations by Seneviratne *et al* (2010) and Greve *et al* (2014) show that regions with reduced precipitation would become water limited and thus may observe a negative trend in *ET*, as reported by Jung *et al* (2010) (-0.79 mm yr^{-1} between 1998 and 2008). Overall, most of the studies reported notable increasing trends towards the end of the 20th century (∼1980–2000), which weakened in the early 21st century (∼2000–2010). The variation in reported *ET* trends can be attributed to the different methodologies used for *ET* estimation, including water budget-based, remote sensing-based, machine learning-based, LSMs and hybrid models. Recently, Tang *et al* (2024) provided a comprehensive comparison of 25 different global *ET* products covering the period from ∼2001–2018 and found that most products consistently capture global spatial distributions of annual *ET* trends. Based on this comprehensive analysis, the increasing trend is considered realistic with a high probability, as also suggested by the IPCC report (Douville *et al* 2021).

To check if KF-ET follows the expected trend, significant Sen's slope (alpha = 0.05) is computed (figure 4(b)). The area-weighted global mean value of Sen's slope is 0.18 ± 0.02 mm yr^{-1} over the land, which hints towards a consistent increase in *ET* between 2003 and 2016. When a similar analysis is conducted using Fluxcom and ERA5 data sets, the *ET* trends are -0.018 ± 0.01 mm yr^{-1} and -0.021 ± 0.01 mm yr^{-1}, respectively, which is an order of magnitude smaller and with a different sign. This disparity in *ET* trends and their magnitude aligns with the findings of Anabalón and Sharma (2017). Reiterating a recurrent observation, reanalysis data sets generally struggle to capture *ET* trends (Mao and Wang 2017). The global mean trends from our KF-ET product compare well with Hobeichi *et al* (2021), where they analyzed *ET* products obtained by optimally combining several observations. Notably, the observed KF-ET trend of 0.18 mm yr^{-1}, while consistent, is smaller compared to the long-term trend of 0.54 mm yr^{-1} (between 1980 and 2012) reported by Anabalón and Sharma (2017). Although a net positive area-weighted global trend is observed in KF-ET, some regions have a negative slope, and many regions have no slope, which is due to spatially varying wetting and drying trends due to climate change and human intervention in response to anomalous regional water availability (Zhang *et al* 2016, Hobeichi *et al* 2021). The global average of KF-ET is increasing with time due to increasing atmospheric demand, which is expected for a warming Earth (Novick *et al* 2016, Guldberg *et al* 2018, Vicente-Serrano *et al* 2020, Douville *et al* 2021, Lian *et al* 2021). There is a positive trend in the Amazon and Ganges basins, which is consistent with regional studies that have attributed these trends to changes in vegetation, meteorological variables, increasing atmospheric water vapor demand, and irrigation practices (Tuinenburg *et al* 2012, Zhang *et al* 2016, Shah *et al* 2019, Heerspink *et al* 2020, Pan *et al* 2020, Baker *et al* 2021, Tang *et al* 2024).

Regions with higher variability are expected to experience larger trends. The standard deviations of the *ET* time-series from KF-ET, Fluxcom and ERA5 are shown in figures 4(a), (c) and (e). It shows similar spatial patterns but with higher amplitudes for KF-ET compared to the other two for North America, Europe, Australia and Africa. Notably, distinct patterns emerge in South America and the

Indian subcontinent, revealing substantial differences between KF-ET and Fluxcomm/ERA5, which were discussed in sections 5.1 and 5.2. Sen's slope values for KF-ET range from -2.88 to $+4.57$ mm yr^{-1}. To better attribute the rate of change in *ET*, Sen's slope is analyzed in conjunction with LULC classes, Köppen climate zones and various elevation groups (figures F3(a)–(c) in appendix F). The Sen's slope values have the largest range in savannas and natural vegetation, followed by grasslands, shrublands and forests, and the lowest in the wetlands and snow-ice LULC classes. Among the vegetation-based classes, forests exhibit the lowest variation in Sen's slope, which could be attributed to their ability to regulate *ET* as per their needs. Limited access to deep water could be a potential limiting factor for the savannas, natural vegetation, grasslands, and shrublands. These classes are sensitive to changes in water availability (Hou *et al* 2022). Similarly, for the Köppen climatic zones (figure F3(b)), the variations are the highest in tropical followed by the temperate and arid regions, while the lowest is in the cold and polar regions. This may be due to multiple factors, such as the tropics commanding the highest area globally and hosting the most varied landscapes, from deserts in the African continent to the rainforest in the Indian subcontinent. Finally, the influx of incoming solar energy is also the highest in the tropics. All the elevation groups showed a similar range of Sen's slope values up to 1500 m elevation levels (figure F3(c)). The higher elevation zone ($\geqslant$1500 m) tends to have lower Sen's slope values. Most of these higher elevation zones are categorized under cold regions, which show consistent patterns, and thus, almost no trend is observed in *ET*.

5.4. Strengths and limitations

A robust water budget-based *ET* product is developed that has small uncertainty and captures the anthropogenic fingerprint of *ET*,which cannot be obtained via existing model-based, radiation-based and hybrid *ET* products. This data set can be used as a benchmark to evaluate other *ET* data sets on similar spatial and temporal scales. The independence of KF-ET from any single input in the combination and its robustness against outliers, ingestion sequences, inflated uncertainties, and initial values are significant advantages (appendix B). KF-ET performs consistently well in comparison to established data sets, including Fluxnet, Fluxcom, ERA5, WA-ET, WGHM and GLEAM *ET* products. This deviated from where other data sets were expected to fail due to limitations in accounting for irrigation and modeling forest zones.

The methodology has two major limitations. First, the resolution of the output data is limited by the resolution of the input data, which may restrict its application to local scale studies. The spatial and temporal resolutions of GRACE data, along with the gap between GRACE and GRACE-FO limit the extent, spatiotemporal resolution and the accuracy of the product. The second is the lack of a comprehensive global validation. Comparison against other products is not a real validation because ground truth is not available. The selected Fluxnet sites are point data and the coarse resolution of KF-ET requires the fluxnet site to be a good representative of a $1^\circ \times 1^\circ$ grid cell, which is physically not plausible due to the highly dynamic nature of *ET*. Therefore, only a few sites could be selected that have more than one-third of the grid cell as a homogenous LULC class. As the fraction of the homogeneous LULC increases, the agreement between KF-ET and Fluxnet data improves (figure E1 in appendix E). Nevertheless, this is probably the first comprehensive attempt at deriving *ET* products that also contain human signatures.

6. Conclusion

Estimating *ET* is vital for understanding the changes in the water cycle, but it remains elusive. *ET* from models and satellite observations have huge uncertainty. Therefore, using water budget-based methods is an exciting alternative. However, there are several global products for water-cycle components, resulting in thousands of *ET* estimates with a large spread. To tackle this problem, the Kalman filter is used in this study. The output (KF-ET) from ingesting various water budget-based *ET* in a Kalman filter is heavily data driven and is not affected by the *ET* used for initialization and a few outliers. The final KF-ET product has an uncertainty of $<$2 mm/month and agrees well with Fluxnet data where a homogeneous LULC type model is dominant over a grid cell. KF-ET is able to capture the interannual and seasonal variability better than model-based and reanalysis products, such as VIC and ERA5. This is because water budget-based *ET* captures the variability induced by interannual and seasonal variations in precipitation as well as human-driven storage changes. Hence, the method proposed accounts for intricate feedback mechanisms operating in both the atmospheric and subsurface domains, as well as human interventions, such as groundwater abstraction and reservoir filling. The efficacy of KF-ET in capturing irrigation signals is demonstrated over the Ganges via simulations that account for irrigation and complex cropping patterns. Similarly, over the Amazon basin, KF-ET exhibits better performance in capturing seasonal variability, even in the presence of intricate driving forces, such as energy, water dynamics, vegetation response and their interactions. The area-weighted global mean of Sen's slope values over land for KF-ET is 0.18 ± 0.02 mm yr^{-1}, which corroborates the expected behavior due to climate change and also compares well with other recent studies that used sophisticated data assimilation approaches to estimate *ET* trends. This study provides a simple Kalman filter-based framework to ingest water budget-based estimates of ET to deliver a data-driven ET that captures natural and human-caused variability conclusively. The KF-ET product is openly available at https://doi.org/10.6084/m9.figshare.23800692.

Data availability statement

The data that support the findings of this study are openly available at the following URL/DOI: https://doi.org/10.6084/m9.figshare.23800692.

All the data sets used in the study are open-source and freely accessible to everyone (details in table 1). The Global Monthly ET product (KF-ET) generated in this study is freely available at the above URL.

Climate Data Operator (CDO), NCAR Command Language (NCL), Python 3 and Matlab 2022a are used for routine implementation of methodology and generation of figures.

The codes utilized in this manuscript are available at https://github.com/gshubham44/KF-ET

Acknowledgments

S G, C R T, R K, N S P, V K Y, A and J J acknowledge the MHRD PhD Fellowships provided by the Ministry of Education, Government of India.

Conflict of interest

The authors declare that they have no known competing financial interests or personal relationships that could have appeared to influence the work reported in this manuscript.

Appendix A. Details about Kalman filter, KF-ET and it is uncertainties

Kalman showed that if multiple observations of the same variable with corresponding uncertainties are available, then the Kalman filter algorithm will reduce the noise and estimate the true value of the variable (Kalman 1960). Let us consider a linear system represented as,

$$x_n = A x_{n-1} + w_n, \tag{A.1}$$

with measurements given by,

$$y_n = C x_n + v_n. \tag{A.2}$$

Here, x represents the state, y is the measurement available from some source, w is the process noise, v is the measurement error or the uncertainty, A is the state transition matrix, C operator relates to state x with measurements y. The process noise is assumed to have a zero mean random distribution, and it is used to compute an error variance-covariance matrix W that is a positive definite matrix. R is a positive definite matrix representing zero mean random error in the measurement. n is the state. The optimal estimate of x can then be recursively generated as,

$$\hat{x}_{n|n} = \hat{x}_{n|n-1} + Q_{n|n-1} C^T \left[C Q_{n|n-1} C^T + R_n \right]^{-1} \times \left(y_n - C \hat{x}_{n|n-1} \right). \tag{A.3}$$

Here, $Q_{n|n-1}$ is the error covariance of $\hat{x}_{n|n-1}$ that is also generated recursively using the following:

$$Q_{n|n} = Q_{n|n-1} I - Q_{n|n-1} C^T \times \left[C Q_{n|n-1} C^T + R \right]^{-1} C Q_{n|n-1}. \tag{A.4}$$

When the state n corresponds to time, then the Kalman filter is in predictive mode. In this study, it as a filter that approaches true ET by including various water budget-based ET. Hence, n denotes the number of various ET estimates available from the water budget.

In this study, a recursive approach using the Kalman filter was employed to handle multiple observations of ET. Here, water budget-based ET is estimated for each grid at each time step and these water budget-based ET estimates are considered to be ET observations to feed to the Kalman filter. Unlike traditional recursive methods that update the ET estimate over time, the approach used here iteratively updates the prior ET estimate using 96 individual ET observations. In each iteration, the prior ET estimate is updated with one of the 96 ET observations. The updated ET estimate then serves as the prior estimate for the subsequent iteration, and this process continues until all 96 ET observations have been utilized. This recursive procedure enables iterative refinement of the ET estimate using multiple observations, resulting in a more accurate and comprehensive estimation of ET. Here, the Kalman filter was utilized independently as a filter at each grid cell (13 666 grids with 1° resolution) and each time step (168 monthly time steps from 2003–2016). Consequently, the procedure was employed 2295 888 times (i.e. 13 666 grids * 168 time steps). The detailed step-by-step procedure is presented in table A1.

The inputs to the Kalman filter included 96 water budget-based ET estimates (ET_i, where $i = 1$ to 96), their corresponding uncertainties (UET_i, where $i = 1$ to 96), initial values (ET_0) and the corresponding uncertainty (UET_0). The 96 ET estimates and the uncertainties correspond to column 2 and 3 of table A1, while the updated ETs and their uncertainties are found in columns 5 and 6, respectively. The Kalman gain (KG), calculated at each of the 96 iterations is presented in column 4. The equations used at each iteration are also presented in table A1 for clarity. The process begins with the calculation of KG, followed by the updated ET (ET_u) and its uncertainties (UET_u). The results from the 96th iteration (i.e. ET_{96}^u and UET_{96}^u) are the KF-ET value and its uncertainty.

Table A1. Step-by-step derivation of KF-ET using 96 water budget-based *ET* estimates and its corresponding uncertainties.

Iter. No	ET	UET	KG	ET^u	UET^u
				ET_0 (Initialization)	UET_0 (Initialization)
1	ET_1	UET_1	$KG_1 = UET_0/(UET_0 + UET_1)$	$ET_1^u = ET_0 + KG_1 \times (ET_1\text{-}ET_0)$	$UET_1^u = (1 - KG_1) \times UET_0)$
2	ET_2	UET_2	$KG_2 = UET_1^u/(UET_1^u + UET_2)$	$ET_2^u = ET_1^u + KG_2 \times (ET_2\text{-}ET_1^u)$	$UET_2^u = (1\text{-}KG_2) \times UET_1^u)$
3	ET_3	UET_3	$KG_3 = UET_2^u/(UET_2^u + UET_3)$	$ET_3^u = ET_2^u + KG_3 \times (ET_3\text{-}ET_2^u)$	$UET_3^u = (1\text{-}KG_3) \times UET_2^u)$
…	…	…	…	…	…
…	…	…	…	…	…
…	…	…	…	…	…
94	ET_{94}	UET_{94}	$KG_{94} = UET_{93}^u/(UET_{93}^u + UET_{94})$	$ET_{94}^u = ET_{93}^u + KG_{94} \times (ET_{94}\text{-}ET_{93}^u)$	$UET_{94}^u = (1\text{-}KG_{94}) \times UET_{93}^u)$
95	ET_{95}	UET_{95}	$KG_{95} = UET_{94}^u/(UET_{94}^u + UET_{95})$	$ET_{95}^u = ET_{94}^u + KG_{95} \times (ET_{95}\text{-}ET_{94}^u)$	$UET_{95}^u = (1\text{-}KG_{95}) \times UET_{94}^u)$
96	ET_{96}	UET_{96}	$KG_{96} = UET_{95}^u/(UET_{95}^u + UET_{96})$	$ET_{96}^u = ET_{95}^u + KG_{96} \times (ET_{96}\text{-}ET_{95}^u)$	$UET_{96}^u = (1\text{-}KG_{96}) \times UET_{95}^u)$

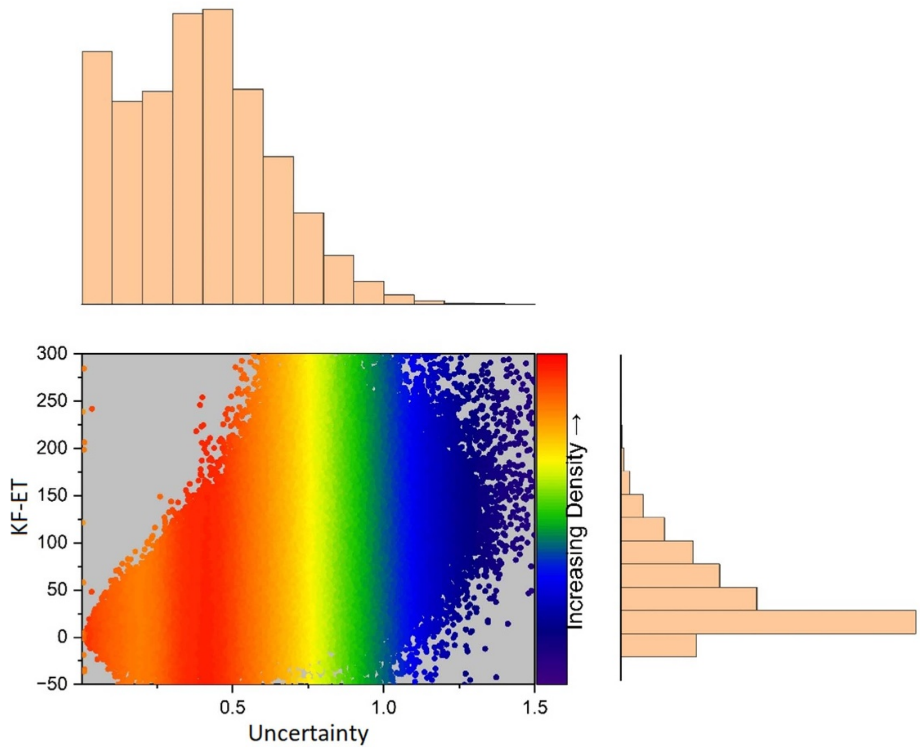

Figure A1. Density-density scatterplot of KF-ET and corresponding uncertainties for all the years 2003–2016 at monthly scales (mm/month).

In this study, the initial values (ET_0 and UET_0) were derived from ERA5 *ET* data.

A 2D density plot is analyzed to check the relation between KF-ET and its corresponding uncertainties for all the years (figure A1). After aggregation across all the grids and time scales, a positively skewed distribution can be seen for both *ET* and the uncertainty. For both quantities, the lower values have higher density and as the values increases density diminishes. Also with a positive relation, the uncertainty tends to increase with increasing *ET* values.

Appendix B. Quick convergence and robustness of KF-ET

At most locations, KF-ET converges quickly and the number of *ET* combinations required to achieve an uncertainty $<2\,\mathrm{mm\,month^{-1}}$ for the entire study period is less than 30. This can be further verified in figure B1(a), which represents the spatial variation of the number of combinations required for different months in year 2003. Relatively higher combinations are required for months with higher *ET*, which is in accordance with figure A1. For all years considered in this study, the KF-ET convergence patterns are found to be similar (figure B1(b)).

In addition, the robustness of the methodology was evaluated through three approaches. First, for data sets without the ensemble-based uncertainties (table 1), uncertainties were inflated (assumed 100% of the value) to assess the convergence and performance of KF-ET. Second, the order of ingestion of 96 *ET* estimates was randomized to examine whether the sequence influenced the final KF-ET estimate.

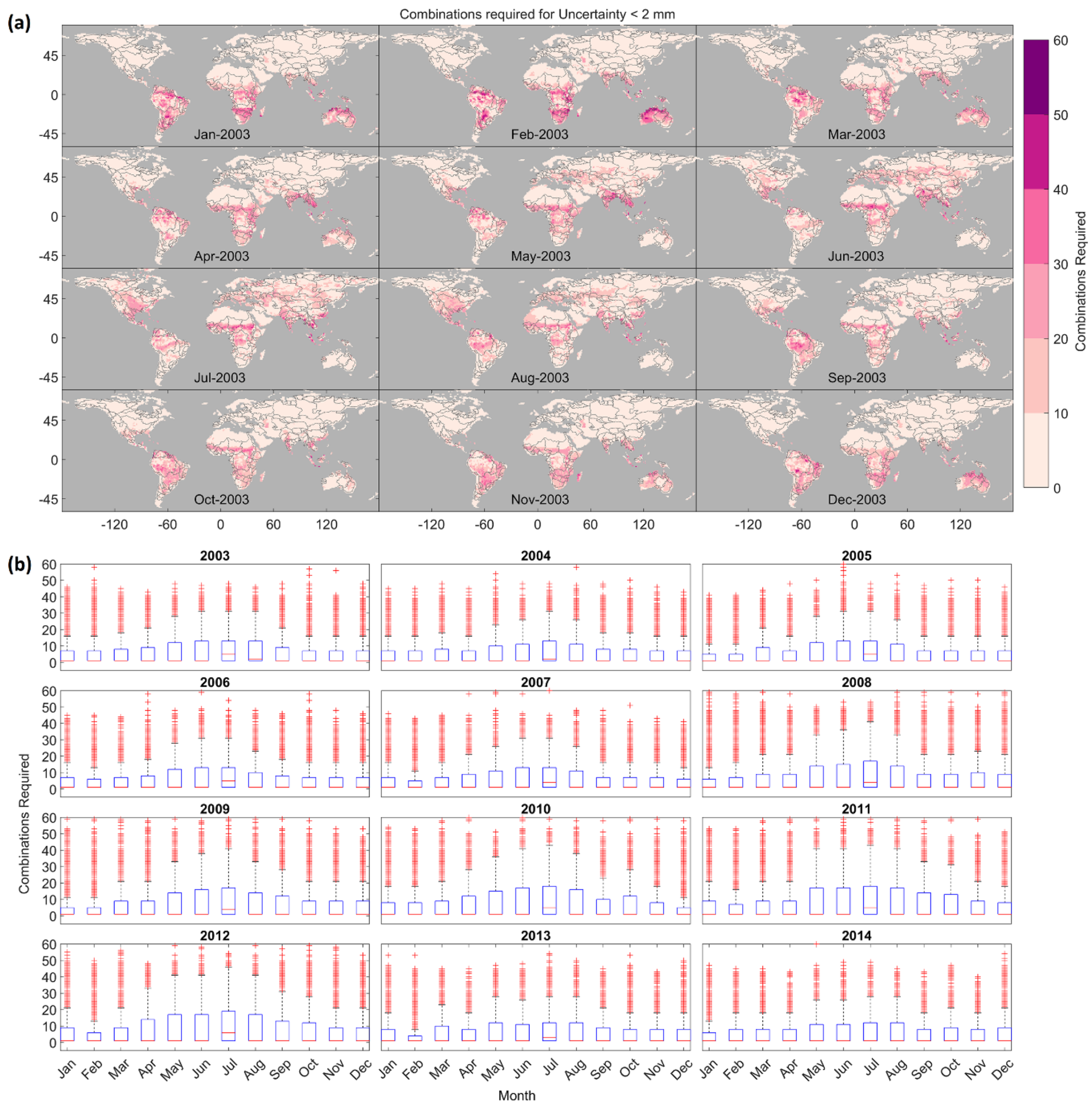

Figure B1. (a) Number of combinations required in KF-ET computation to achieve uncertainty <2 mm month^{-1} for the year 2003 and (b) spatially aggregated box plot for years 2003–2014.

In most grids, KF-ET converged quickly (around 30 observations, figure B1) with an uncertainty of < 2 mm month^{-1}, demonstrating that convergence was independent of both the inflated uncertainty in the input data and the sequence of observation ingestion. Finally, to test the robustness of the proposed methodology, two additional cases were evaluated with different initializations. For Case-1 the initial values from ERA5 *ET* were replaced with GLEAM *ET* data. In Case-2, initial values from ERA5 *ET* were replaced with one of the 96 water budget *ET* estimates and ERA5 *ET* was considered as one of the observations. The results from the two cases with different initializations consistently converged to the same KF-ET values (figure B2). This substitution confirmed that the methodology is resilient to changes in initial values. Consequently, the methodology demonstrated robustness against outliers, sequence of ingestion, inflated uncertainties, and initial values.

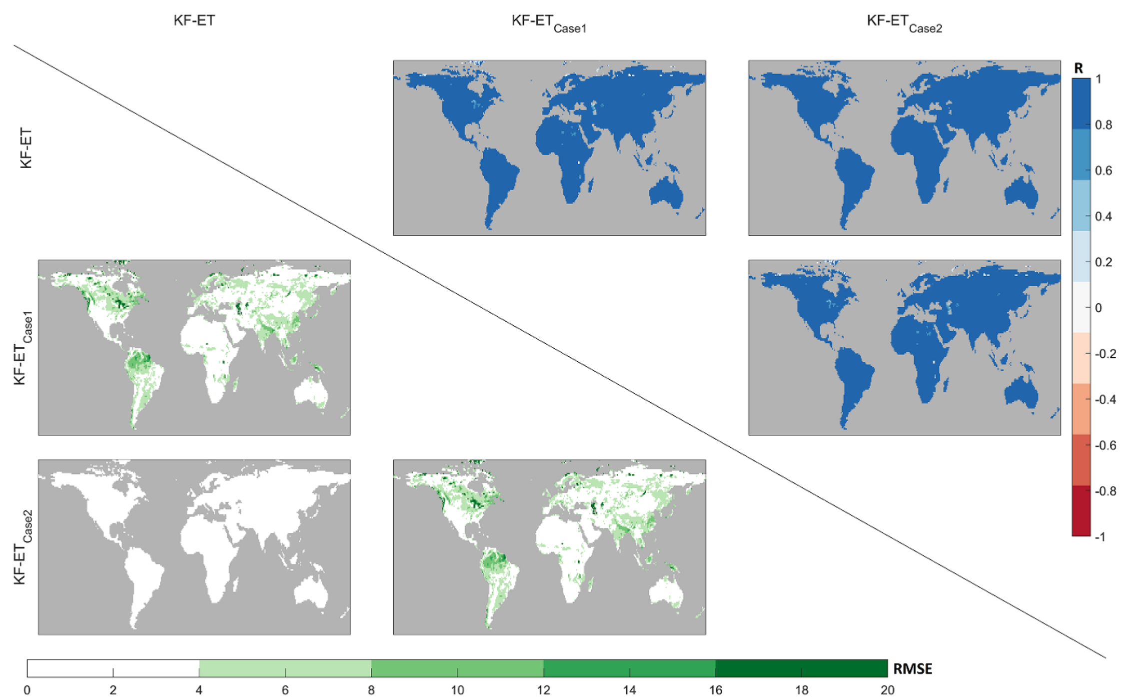

Figure B2. Comparison of Kalman filter-based *ET* estimates: (i) initialization with ERA5 *ET* (KF-ET), (ii) initialization with GLEAM *ET* (Case-1) and (iii) initialization with one of the 96 water budget-based *ET*s (Case-2) in terms of *R* (upper triangular matrix) and RMSE (lower triangular matrix).

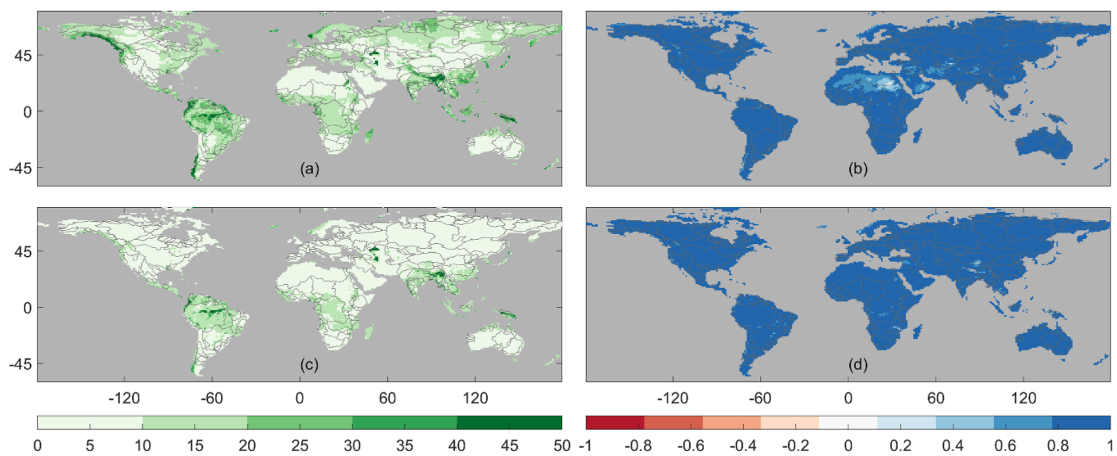

Figure C1. (a) RMSE and (b) correlation between KF-ET and WA-ET; (c) RMSE and (d) correlation between KF-ET and KF-30-ET.

Appendix C. Weighted average computation

For the weighted average computation of 96 *ET* combinations (WA-ET), the weights corresponding to each combination of *ET* is estimated as:

$$w_i = 1/{\sigma_i}^2, \tag{C.1}$$

where σ_i is the propagated uncertainty in the *i*th *ET*. The WA estimate and associated uncertainty of the *ET* can be calculated as follows:

$$\hat{\mu} = \frac{\sum w_i X_i}{\sum w_i}, \text{and} \tag{C.2}$$

$$Var(\hat{\mu}) = \frac{1}{\sum {\sigma_i}^{-2}}. \tag{C.3}$$

The comparison of the *ET* obtained using all 96 combinations via WA-ET and KF-ET are shown in figure C1. It is clear that the two approaches lead to different results. Furthermore, it is also shown that the Kalman filters resulting from only 30 combinations (KF-30-ET) are significantly similar to those obtained using all 96 combinations (KF-ET). This indicates that *ET* from a Kalman filter converges quickly and is stable (figure B1). In other words, output from the Kalman filter-based approach is reliable, even when only a few *ET* pseudo-observations are available.

Appendix D. KF-ET comparison with other global *ET* products

Validation of *ET* is one of the most challenging aspects. There are numerous gridded global *ET* products available but there is no single product that can be used as a benchmark (Tang *et al* 2024). Hence, KF-ET is compared with other extensively used global gridded *ET* products, which are ERA5, GLEAM (Global Land Evaporation Amsterdam Model), WGHM (WaterGAP Global Hydrological Model) and Fluxcom. The comparison of the products in terms of correlation coefficient (R) and root mean squared error (RMSE) at 1° spatial and monthly temporal resolution, resulting in a 5×5 matrix with upper triangular values representing R and lower triangular values representing RMSE is shown in figure D1. The differences between the various *ET* data sets are clearly depicted in figure D1, with the *ET* products performing similarly in some regions, while varying significantly in others. Specifically, regions such as the Amazon, Southern Africa, eastern India and southern China show low correlation and higher RMSE values among products.

A dedicated network of eddy-covariance towers would be required to cover at least a few 1° grid cells, which will be optimal for comparison with KF-ET results. There are only a few regions that have a good network of eddy-covariance towers, but the data is not easily available or openly accessible for all. The Fluxcom product, derived from Fluxnet sites worldwide and assimilated with the MODIS *ET* product, is influenced by the sparse distribution of flux towers in these regions. Consequently, the Fluxcom *ET* values in these areas are predominantly governed by the MODIS *ET*, introducing specific limitations related to calibration degradation, dependence on standard phenology metrices, such as leaf area index (LAI) and enhanced vegetation index (EVI), which are not able to capture photosynthetic dynamics in dense canopies (Wang *et al* 2012, Wu *et al* 2016, Yan *et al* 2016, Ma *et al* 2020, Liu *et al* 2023).

The comparison of all products at the 24 Fluxnet sites is also presented in table D1. While it may initially appear that Fluxcom, ERA5 and KF-ET perform similarly with Fluxcom outperforming at some sites, it is important to note that the Fluxcom product is directly derived from these Fluxnet sites and is thus expected to perform better. It should be noted that WGHM considers various irrigation scenarios and is one of the more reliable hydrology models. Out of four global gridded products considered, KF-ET closely resembles Fluxcom in terms of R and RMSE with exceptions in the Amazon and eastern India. Since the Fluxcom network is dense in Europe and the USA but poor in South America and the Indian subcontinent, it is difficult to judge results in these regions. Although various data sources are available, a fair comparison is not feasible due to scale issues. The KF-ET product demonstrates its strengths by

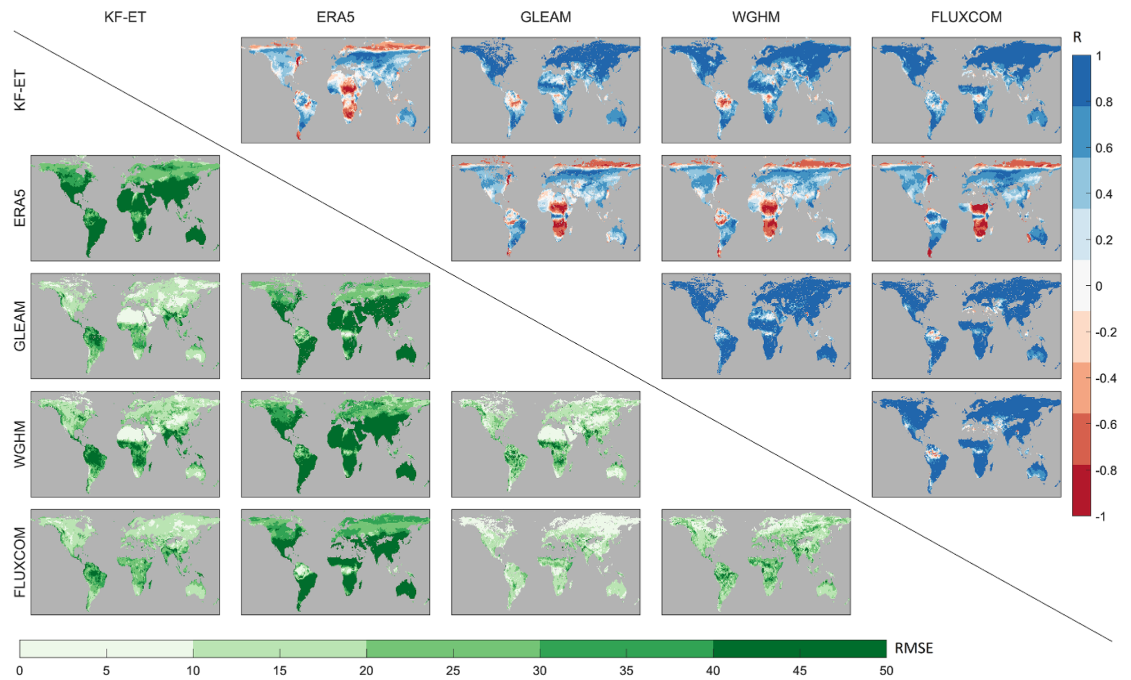

Figure D1. Comparison of *ET* from KF-ET, ERA5, GLEAM, WGHM and FLUXCOM in terms of R (upper triangular matrix) and RMSE (lower triangular matrix).

Table D1. Comparison of KF-ET, WA-ET, ERA5, Fluxcom, GLEAM and WGHM with respect to Fluxnet sites in terms of Nash–Sutcliffe Efficiency (NSE). (ENF-Evergreen Needle leaf Forest; GRA-Grassland; CRO-Cropland; MF-Mixed Forest; WSA-Woody Savannas; SAV-Savannas; EBF-Evergreen Broad leaf) Forest.

ID	Name	Dominant LULC	Dominant LULC (%)	Data available (%)	Latitude	Longitude	KF-ET	WA-ET	ERA5	Fluxcom	GLEAM	WGHM
124	US-Ne2	CRO	97	92	41.17	−96.48	0.68	0.61	0.74	0.75	0.28	−0.05
30	CA-Gro	MF	93	100	48.22	−82.16	0.72	0.50	0.81	0.84	0.24	0.19
72	FR-Gri	CRO	92	92	48.84	1.95	0.63	0.43	0.68	0.61	0.74	0.45
32	CA-SF1	ENF	88	33	54.49	−105.82	0.49	0.49	0.49	0.56	0.38	0.24
67	FI-Hyy	ENF	87	95	61.85	24.29	0.75	0.20	0.80	0.87	0.33	−0.08
27	BE-Lon	CRO	86	92	50.55	4.75	0.80	0.65	0.79	0.81	0.71	0.54
9	AU-Dry	SAV	84	58	−15.26	132.37	−0.15	−0.51	0.37	0.07	−0.17	−1.71
71	FI-Sod	ENF	82	65	67.36	26.64	0.77	0.19	0.74	0.51	0.25	−0.18
103	US-AR1	GRA	80	33	36.43	−99.42	0.59	0.55	−0.12	0.56	0.59	0.33
56	DE-RuS	CRO	80	31	50.87	6.45	0.60	0.39	0.60	0.59	0.46	0.19
21	AU-Tum	EBF	70	100	−35.66	148.15	0.45	0.09	0.70	0.64	0.32	−0.01
48	DE-Geb	CRO	66	100	51.10	10.91	0.69	0.49	0.67	0.62	0.64	0.05
109	US-Blo	ENF	65	42	38.90	−120.63	−0.30	−0.95	−0.08	0.66	−0.53	−1.05
14	AU-How	WSA	61	92	−12.49	131.15	−1.56	−3.63	0.63	0.32	NaN	−1.00
132	US-Syv	MF	54	49	46.24	−89.35	0.14	−0.03	0.16	0.00	NaN	−0.30
121	US-Me2	ENF	48	100	44.58	−121.50	−0.70	−1.86	0.37	0.82	0.50	0.16
130	US-SRG	GRA	48	58	31.79	−110.83	0.63	0.37	0.66	0.78	0.46	−0.05
73	FR-LBr	ENF	48	50	44.72	−0.77	0.69	0.35	0.84	0.63	0.71	0.23
51	DE-Kli	CRO	48	91	50.89	13.52	0.71	0.46	0.74	0.67	0.65	0.21
22	AU-Wac	EBF	48	33	−37.43	145.19	0.00	−0.72	−0.04	0.62	NaN	−0.40
113	US-GLE	ENF	39	90	41.37	−106.24	−1.54	−2.21	−0.40	−0.36	−1.44	−2.08
69	FI-Let	ENF	39	33	60.64	23.96	0.28	−0.18	0.31	0.33	0.10	−0.90
41	CH-Dav	ENF	33	92	46.82	9.86	−0.26	−0.64	0.45	0.60	0.37	−1.25
5	AU-Cpr	SAV	31	40	−34.00	140.59	−0.21	−0.68	−1.50	0.32	−0.14	−0.65

closing the water budget in regions where Fluxnet sites are sparse, such as the Amazon, eastern India and southern China.

Appendix E. Fluxnet data preparation and scale issues

The authors started with the whole Fluxnet 2015 open access data set (fluxnet.fluxdata.org) consisting of 267 sites across the globe, which are non-uniformly distributed with a large fraction of sites located in the USA, Europe and Australia. There is a major challenge in comparing site-based observations from flux tower to the 1° gridded KF-ET product due to the substantial difference in spatial scale, the dominant LULC classes and the timeframe of available data. For a fair comparison, 24 Fluxnet sites (table D1) were selected from 267 sites. The choice of these sites was based on various filtering criteria. First, it involved the similarity between the LULC class of Fluxnet site and the dominant LULC class of KF-ET within the 1° grid. Second, it involved selection of sites with 30% or more usable data between the timeframe 2003–2016. Although this ensured that the dominant LULC influencing KF-ET is consistent with the Fluxnet site LULC type, since KF-ET is the resultant ET estimates of all LULC classes within that grid, which can have large deviations in *ET* when compared to the Fluxnet site.

More details about the preprocessing involved in the data set can be found in Pastorello *et al* (2020). Based on the data-disseminating website (fluxnet.org/data/fluxnet2015-dataset/data-processing/), the gap filling of the site level measurements have been done using the multidimensional scaling method, as described in Reichstein *et al* (2005). Data availability (%) is based on the available monthly values from January 2003–December 2013. For comparison with KF-ET, Fluxnet data were filtered with a moving average.

The raw Fluxnet data set for 24 sites (table in D1) used in this study is provided at the link https://doi.org/10.6084/m9.figshare.23800692.

The dominant LULC class percentage influences the NSE value between the Fluxnet site and KF-ET. This makes the choice of sites even more difficult and sparse. As expected, and as can be seen in figure E1, the NSE varies linearly with the increase in the dominant LULC class percentage. This analysis reiterates the fact that the comparison between site scale and 1° grid scale is challenging.

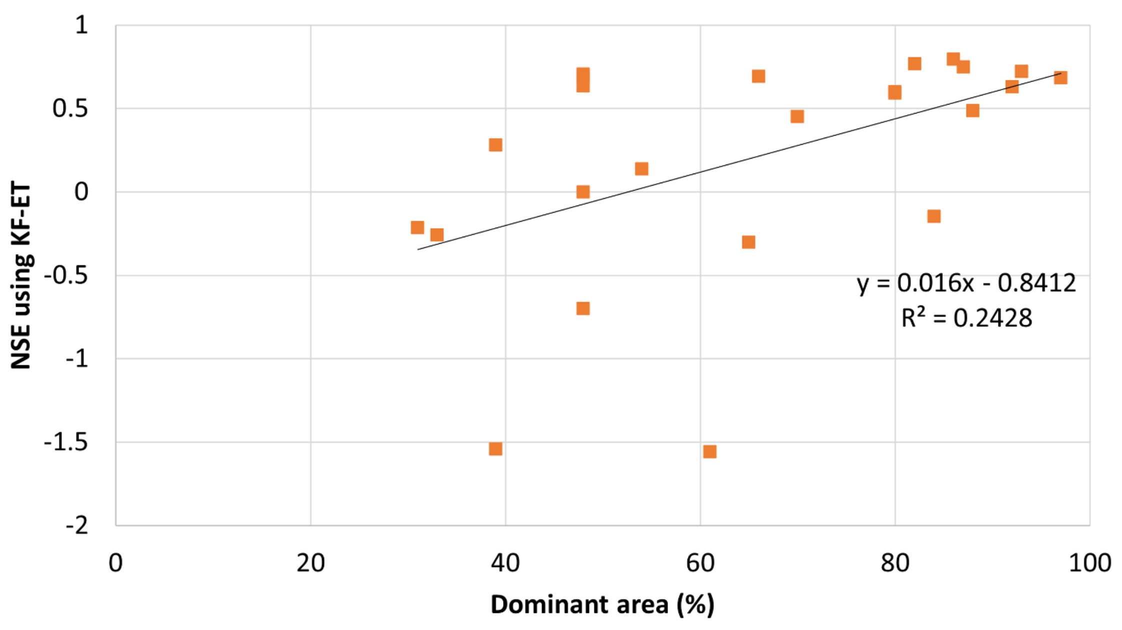

Figure E1. Variation of NSE at the 24 Fluxnet sites using KF-ET with respect to the dominant LULC class percentage.

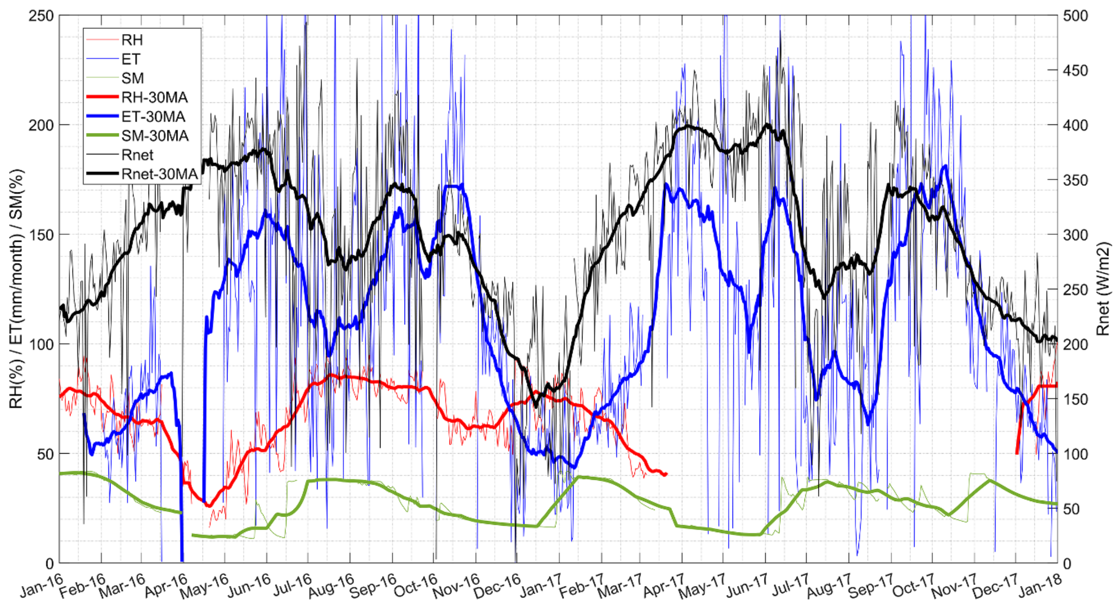

Figure F1. Time-series of daily and 30 day moving average of *in- situ* measurements of net radiation, relative humidity, *ET* and soil moisture at a site in Kanpur, India, from the INCOMPASS data set.

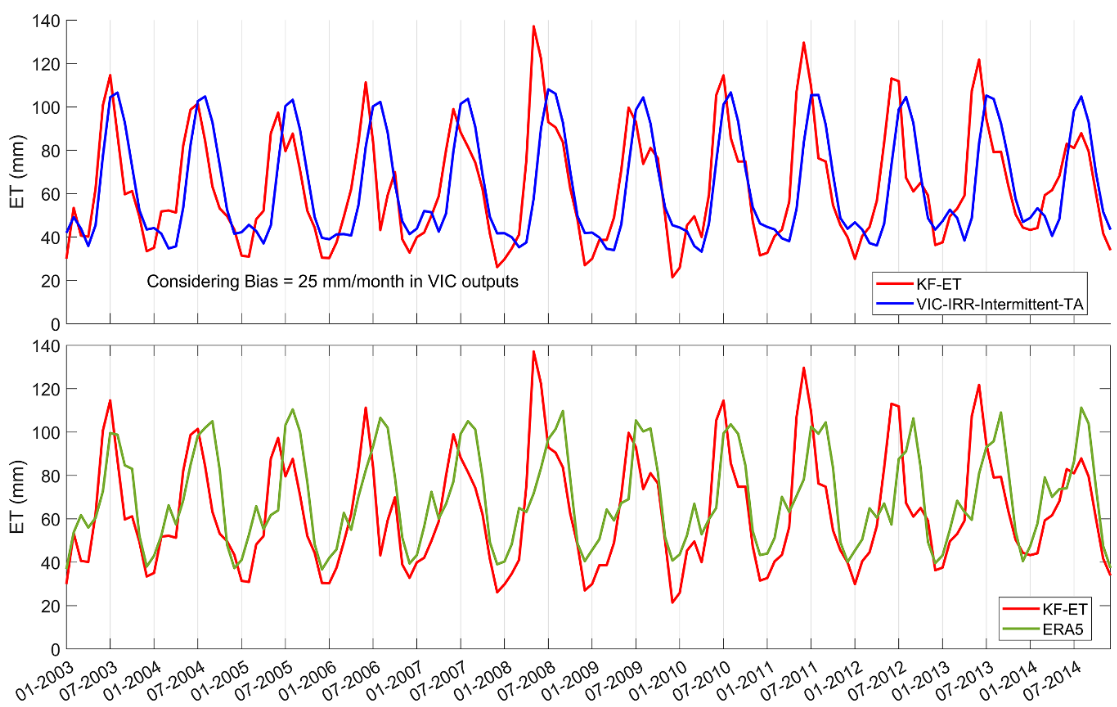

Figure F2. Time-series of averaged *ET* (mm/month) estimated using (a) KF-ET and VIC-IRR-Intermittent-TA; (b) KF-ET and ERA5.

Appendix F. VIC simulation in the Ganges and trend analysis with LULC, climate and elevation groups

The plot of fluxes from the Kanpur site (Ganges basin) in India is plotted in figure F1 (Morrison *et al* 2019). Further detailed comparison of *ET* in the Ganges basin between KF-ET, ERA5 and VIC-IRR-Intermittent-TA is shown in figure F2. The VIC simulation results are taken from already published articles (Joseph *et al* 2022, Joseph and Ghosh 2023). These studies have incorporated a flood irrigation module in the VIC model to represent the irrigation practices used for paddy cultivation in the Ganges River basin. Joseph and Ghosh (2023) describes in detail the VIC model modification, setup,

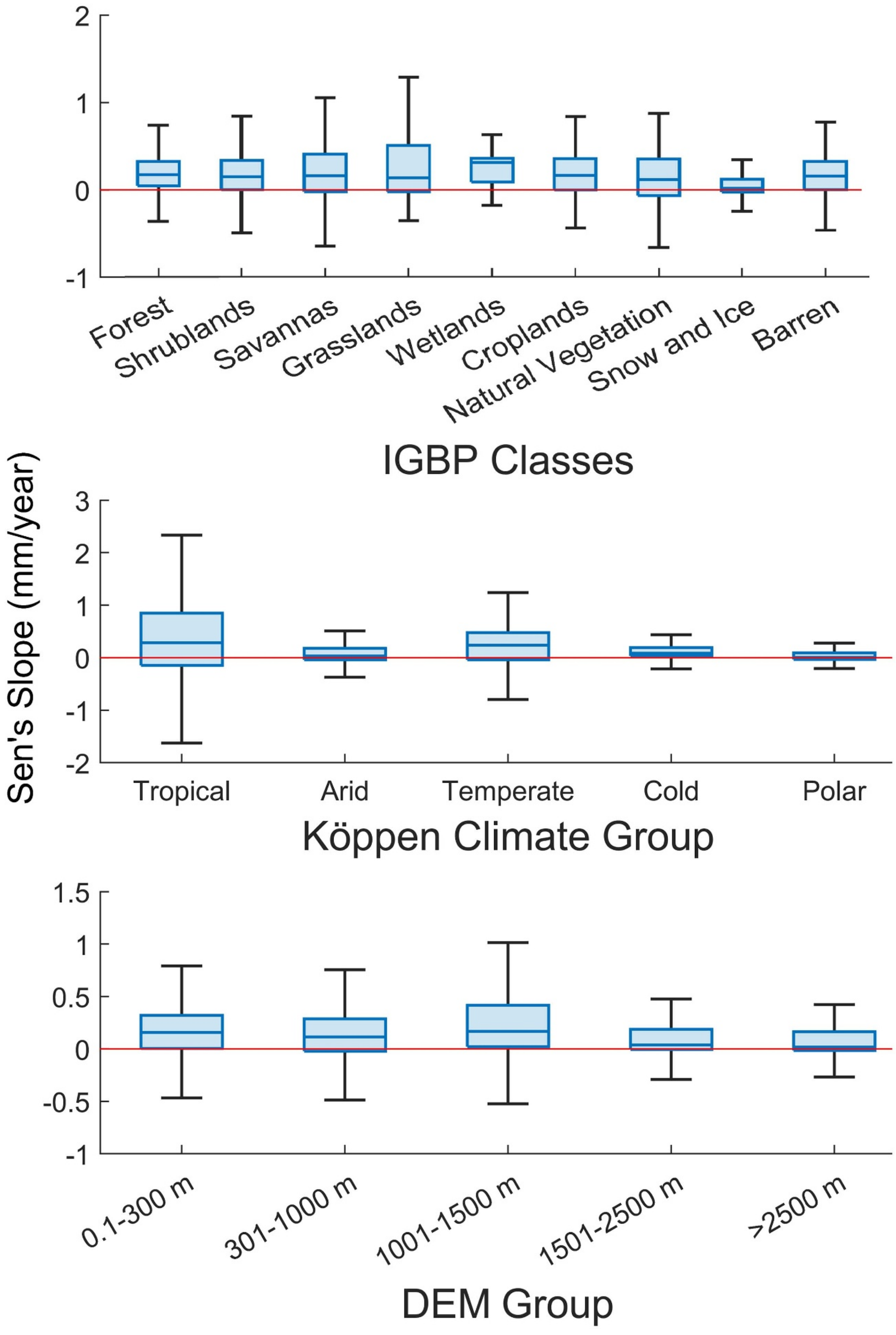

Figure F3. Variation of Sen's slope based on various (a) IGBP land use land cover classes, (b) Köppen climate groups and (c) elevation groups.

calibration and validation. They observed overall improved performance of VIC-IRR (VIC with irrigation module) compared to the VIC model in terms of soil moisture, *ET* as well as streamflow. Further global analysis of the trends on basis of LULC classes, climate and elevation groups is detailed in figure F3.

ORCID iDs

Shubham Goswami https://orcid.org/0000-0002-8118-2453
Chirag Rajendra Ternikar https://orcid.org/0000-0002-5977-3396

Vivek Kumar Yadav https://orcid.org/0009-0000-7156-4450
Bramha Dutt Vishwakarma https://orcid.org/0000-0003-4787-8470

References

Allen R, Pereira L, Raes D and Smith M 1998 Crop evapotranspiration-guidelines for computing crop water requirements *FAO Irrigation and drainage paper 56* 300 D05109 (available at: www.fao.org/4/X0490E/X0490E00.htm)

Allen R and Pruitt W 1986 Rational use of the fao Blaney-Criddle formula *J. Irrig. Drain. Eng.* **112** 139–55

Anabalón A and Sharma A 2017 On the divergence of potential and actual evapotranspiration trends: an assessment across alternate global datasets *Earth's Future* **5** 905–17

Badgley G, Fisher J B, Jiménez C, Tu K P and Vinukollu R 2015 On uncertainty in global terrestrial evapotranspiration estimates from choice of input forcing datasets *J. Hydrometeorol.* **16** 1449–55

Baker J C, Garcia-Carreras L, Gloor M, Marsham J H, Buermann W, da Rocha H R, Nobre A D, de Araujo A C and Spracklen D V 2021 Evapotranspiration in the amazon: spatial patterns, seasonality and recent trends in observations, reanalysis and climate models *Hydrol. Earth Syst. Sci.* **25** 2279–300

Beaudoing H and Rodell M 2020a GLDAS Noah Land Surface Model L4 monthly 0.25 × 0.25 degree V2.1, Greenbelt, Maryland, USA Goddard Earth Sciences Data and Information Services Center (GES DISC) (https://doi.org/10.5067/9SQ1B3ZXP2C5)

Beaudoing H and Rodell M 2020b GLDAS VIC Land Surface Model L4 monthly 1.0 × 1.0 degree V2.1, Greenbelt, Maryland, USA Goddard Earth Sciences Data and Information Services Center (GES DISC) (https://doi.org/10.5067/VWTH7S6218SG)

Beck H, Zimmermann N, McVicar T, Vergopolan N, Berg A and Wood E 2018 Present and future Köppen-Geiger climate classification maps at 1-km resolution *Sci. Data* **5** 1–12

Bhattarai N, Mallick K, Stuart J, Vishwakarma B D, Niraula R, Sen S and Jain M 2019 An automated multi-model evapotranspiration mapping framework using remotely sensed and reanalysis data *Remote Sens. Environ.* **229** 69–92

Costa M H, Souza-Filho J C and Ribeiro A 2004 Comments on "the regional evapotranspiration of the amazon" *J. Hydrometeorol.* **5** 1279–80

Dorigo W *et al* 2021 Closing the water cycle from observations across scales: where do we stand? *Bull. Am. Meteorol. Soc.* **102** E1897–935

Douville H *et al* 2021 *Water Cycle Changes* (Cambridge University Press) pp 1055–210

Elnashar A, Wang L, Wu B, Zhu W and Zeng H 2021 Synthesis of global actual evapotranspiration from 1982 to 2019 *Earth Syst. Sci. Data* **13** 447–80

Fisher J B *et al* 2017 The future of evapotranspiration: global requirements for ecosystem functioning, carbon and climate feedbacks, agricultural management and water resources *Water Resour. Res.* **53** 2618–26

Gentine P, D'Odorico P, Lintner B, Sivandran G and Salvucci G 2012 Interdependence of climate, soil and vegetation as constrained by the Budyko curve *Geophys. Res. Lett.* **39** 19

Ghiggi G, Humphrey V, Seneviratne S I and Gudmundsson L 2019 Grun: an observation-based global gridded runoff dataset from 1902 to 2014 *Earth Syst. Sci. Data* **11** 1655–74

Ghiggi G, Humphrey V, Seneviratne S I and Gudmundsson L 2021 G-run ensemble: a multi-forcing observation-based global runoff reanalysis *Water Resour. Res.* **57** e2020WR028787

GRDC 2020 Major river basins of the world/global runoff data Q9 centre (GRDC) (Federal Institute of Hydrology) (available at: http://grdc.bafg.de) (Accessed 15 May 2023)

Greve P, Orlowsky B, Mueller B, Sheffield J, Reichstein M and Seneviratne S 2014 Global assessment of trends in wetting and drying over land *Nat. Geosci.* **7** 716–21

Guldberg H *et al* 2018 Impacts of 1.5°C global warming on natural and human systems. Global warming of 1.5°C (IPCC reports) (https://doi.org/10.59327/IPCC/AR6-9789291691647)

Hasler N and Avissar R 2007 What controls evapotranspiration in the amazon basin? *J. Hydrometeorol.* **8** 380–95

Heerspink B, Kendall A, Coe M and Hyndman D 2020 Trends in streamflow, evapotranspiration and groundwater storage across the amazon basin linked to changing precipitation and land cover *J. Hydrol.* **32** 100755

Hersbach H *et al* 2023 Era5 monthly averaged data on single levels from 1940 to present Copernicus Climate Change Service (C3S) Climate Data Store (CDS) (https://doi.org/10.24381/cds.f17050d7)

Hobeichi S, Abramowitz G and Evans J P 2021 Robust historical evapotranspiration trends across climate regimes *Hydrol. Earth Syst. Sci.* **25** 3855–74

Hou H, Zhou B, Pei F, Hu G, Su Z, Zeng Y, Zhang H, Gao Y, Luo M and Li X 2022 Future land use/land cover change has nontrivial and potentially dominant impact on global gross primary productivity *Earth's Future* **10** e2021EF002628

Huffman G J, Bolvin D T, Braithwaite D, Hsu K, Joyce R, Xie P and Yoo S-H 2015 NASA Global Precipitation Measurement (GPM) Integrated Multi-satellite Retrievals for GPM (IMERG) Algorithm Theoretical Basis Document (ATBD) version vol 4 p 30 (available at: http://pmm.nasa.gov/sites/default/files/document_files/IMERG_ATBD_V4.5.pdf)

Jensen M, Burman R and Allen R 1990 Evapotranspiration and irrigation water requirements ASCE Manuals and Reports on Engineering Practices No. 70 (American Society of Civil Engineers)

Joseph J and Ghosh S 2023 Representing indian agricultural practices and paddy cultivation in the variable infiltration capacity model *Water Resour. Res.* **59** e2022WR033612

Joseph J, Scheidegger J M, Jackson C R, Barik B and Ghosh S 2022 Is flood to drip irrigation a solution to groundwater depletion in the indo-gangetic plain? *Environ. Res. Lett.* **17** 104002

Jung M *et al* 2010 Recent decline in the global land evapotranspiration trend due to limited moisture supply *Nature* **467** 951–4

Jung M, Koirala S, Weber U, Ichii K, Gans F, Camps-Valls G, Papale D, Schwalm C, Tramontana G and Reichstein M 2019 The fluxcom ensemble of global land-atmosphere energy fluxes *Sci. Data* **6** 74

Kalman R E 1960 A new approach to linear filtering and prediction problems *J. Basic Eng* **82D** 35–45

Konrad H, Panegrossi G, Bagaglini L, Sanó P, Sikorski T, Cattani E, Schröder M, Mikalsen A and Hollmann R 2022 Precipitation monthly and daily gridded data from 2000 to 2017 derived from satellite microwave observations (Copernicus Climate Data Store) (https://doi.org/10.24381/cds.ada9c583)

Landerer F W and Swenson S 2012 Accuracy of scaled grace terrestrial water storage estimates *Water Resour. Res.* **48** 4

Lehmann F, Vishwakarma B D and Bamber J 2022 How well are we able to close the water budget at the global scale? *Hydrol. Earth Syst. Sci.* **26** 35–54

Li B, Beaudoing H and Rodell M 2020 GLDAS catchment land surface model L4 monthly 1.0 × 1.0 degree V2.1, Greenbelt, Maryland, USA Goddard Earth Sciences Data and Information Services Center (GES DISC) (https://doi.org/10.5067/SGSL3LNKGJWW)

Lian X *et al* 2021 Multifaceted characteristics of dryland aridity changes in a warming world *Nat. Rev. Earth Environ.* **2** 232–50

Liu H, Xin X, Su Z, Zeng Y, Lian T, Li L, Yu S and Zhang H 2023 Intercomparison and evaluation of ten global ET products at site and basin scales *J. Hydrol.* **617** 128887

Liu W, Wang L, Zhou J, Li Y, Sun F, Fu G, Li X and Sang Y-F 2016 A worldwide evaluation of basin-scale evapotranspiration estimates against the water balance method *J. Hydrol.* **538** 82–95

Long D, Longuevergne L and Scanlon B R 2014 Uncertainty in evapotranspiration from land surface modeling, remote sensing and grace satellites *Water Resour. Res.* **50** 1131–51

Lorenz C, Tourian M J, Devaraju B, Sneeuw N and Kunstmann H 2015 Basin-scale runoff prediction: an ensemble Kalman filter framework based on global hydrometeorological data sets *Water Resour. Res.* **51** 8450–75

Loveland T *et al* 2009 ISLSCP II IGBP DISCover and SiB land cover (Oak Ridge National Laboratory Distributed Active Archive Center) (https://doi.org/10.3334/ORNLDAAC/930)

Ma N, Szilagyi J and Jozsa J 2020 Benchmarking large-scale evapotranspiration estimates: a perspective from a calibration-free complementary relationship approach and fluxcom *J. Hydrol.* **590** 125221

Maeda E E, Ma X, Wagner F H, Kim H, Oki T, Eamus D and Huete A 2017 Evapotranspiration seasonality across the amazon basin *Earth Syst. Dyn.* **8** 439–54

Mao Y and Wang K 2017 Comparison of evapotranspiration estimates based on the surface water balance, modified Penman Monteith model and reanalysis data sets for continental China *J. Geophys. Res.* **122** 3228–44

Medvigy D, Wofsy S, Munger J and Moorcroft P 2010 Responses of terrestrial ecosystems and carbon budgets to current and future environmental variability *Proc. Natl Acad. Sci.* **107** 8275–80

Miralles D G, Holmes T, De Jeu R, Gash J, Meesters A and Dolman A 2011 Global land-surface evaporation estimated from satellite-based observations *Hydrol. Earth Syst. Sci.* **15** 453–69

Morrison R, Angadi S S, Cooper H, Evans J, Rees G, Sekhar M, Taylor C, Tripathi S N and Turner A 2019 High temporal resolution meteorology and soil physics observations from INCOMPASS land surface stations in India, 2016 to 2018 (NERC Environmental Information Data Centre) (https://doi.org/10.5285/c5e72461-c61f-4800-8bbf-95c85f74c416)

Mu Q, Zhao M and Running S 2011 Improvements to a modis global terrestrial evapotranspiration algorithm *Remote Sens. Environ.* **115** 1781–800

Munier S, Aires F, Schlaffer S, Prigent C, Papa F, Maisongrande P and Pan M 2014 Combining data sets of satellite retrieved products for basin scale water balance study: 2. Evaluation on the mississippi basin and closure correction model *J. Geophys. Res.* **119** 12–100

Muñoz-Sabater J *et al* 2021 Era5-land: a state-of-the-art global reanalysis dataset for land applications *Earth Syst. Sci. Data* **13** 4349–83

Novick K *et al* 2016 The increasing importance of atmospheric demand for ecosystem water and carbon fluxes *Nat. Clim. Change* **6** 1023–7

O'Connor J, Santos M J, Rebel K T and Dekker S C 2019 The influence of water table depth on evapotranspiration in the amazon arc of deforestation *Hydrol. Earth Syst. Sci.* **23** 3917–31

Paca V H d M, Espinoza-Dávalos G E, Hessels T M, Moreira D M, Comair G F and Bastiaanssen W G 2019 The spatial variability of actual evapotranspiration across the Amazon River basin based on remote sensing products validated with flux towers *Ecol. Process.* **8** 1–20

Pan M and Wood E F 2006 Data assimilation for estimating the terrestrial water budget using a constrained ensemble Kalman filter *J. Hydrometeorol.* **7** 534–47

Pan M, Wood E F, Wójcik R and McCabe M F 2008 Estimation of regional terrestrial water cycle using multi-sensor remote sensing observations and data assimilation *Remote Sens. Environ.* **112** 1282–94

Pan S *et al* 2020 Evaluation of global terrestrial evapotranspiration using state-of-the-art approaches in remote sensing, machine learning and land surface modeling *Hydrol. Earth Syst. Sci.* **24** 1485–509

Pastorello G *et al* 2020 The fluxnet2015 dataset and the oneflux processing pipeline for eddy covariance data *Sci. Data* **7** 225

Penman H 1948 Natural evaporation from open water, bare soil and grass *Proc. R. Soc.* **193** 120–45

Reichstein M *et al* 2005 On the separation of net ecosystem exchange into assimilation and ecosystem respiration: review and improved algorithm *Glob. Change Biol.* **11** 1424–39

Rodell M *et al* 2004 The global land data assimilation system *Bull. Am. Meteorol. Soc.* **85** 381–94

Rodell M, McWilliams E B, Famiglietti J S, Beaudoing H K and Nigro J 2011 Estimating evapotranspiration using an observation based terrestrial water budget *Hydrol. Process.* **25** 4082–92

Rougier J, Brady A, Bamber J, Chuter S, Royston S, Vishwakarma B D, Westaway R and Ziegler Y 2023 The scope of the Kalman filter for spatio-temporal applications in environmental science *Environmetrics* **34** e2773

Rustemeier E, Hänsel S, Finger P, Schneider U and Ziese M 2022 GPCC climatology version 2022 at 0.5°: monthly land-surface precipitation climatology for every month and the total year from rain-gauges built on GTS-based and historical data (https://doi.org/10.5676/DWD_GPCC/FD_M_V2022_250)

Saleska S *et al* 2003 Carbon in amazon forests: unexpected seasonal fluxes and disturbance-induced losses *Science* **302** 1554–7

Seneviratne S, Corti T, Davin E, Hirschi M, Jaeger E, Lehner I, Orlowsky B and Teuling A 2010 Investigating soil moisture-climate interactions in a changing climate: a review *Earth-Sci. Rev.* **99** 125–61

Shah H, Zhou T, Huang M and Mishra V 2019 Strong influence of irrigation on water budget and land surface temperature in indian subcontinental river basins *J. Geophys. Res.* **124** 1449–62

Shao X, Zhang Y, Liu C, Chiew F H, Tian J, Ma N and Zhang X 2022 Can indirect evaluation methods and their fusion products reduce uncertainty in actual evapotranspiration estimates? *Water Resour. Res.* **58** e2021WR031069

Sinha B K, Hartung J and Knapp G 2011 *Statistical Meta-Analysis With Applications* (Wiley) (https://doi.org/10.1002/9780470386347)

Swann A and Koven C 2017 A direct estimate of the seasonal cycle of evapotranspiration over the Amazon basin *J. Hydrometeorol.* **18** 2173–85

Syed T H, Webster P J and Famiglietti J S 2014 Assessing variability of evapotranspiration over the ganga river basin using water balance computations *Water Resour. Res.* **50** 2551–65

Tang R *et al* 2024 Spatial-temporal patterns of land surface evapotranspiration from global products *Remote Sens. Environ.* **304** 114066

Trenberth K and Stepaniak D 2001 Indices of El Niño evolution *J. Clim.* **14** 1697–701

Tuinenburg O, Hutjes R and Kabat P 2012 The fate of evaporated water from the Ganges basin *J. Geophys. Res.* **117** D1

Verbeeck H, Peylin P, Bacour C, Bonal D, Steppe K and Ciais P 2011 Seasonal patterns of CO_2 fluxes in Amazon forests: fusion of eddy covariance data and the ORCHIDEE model *J. Geophys. Res.* **116** G2

Verdin K, Hall F, Collatz G, Meeson B, Los S, Brown de Colstoun E and Landis D 2011 Islscp II hydro1k elevation-derived products (Oak Ridge National Laboratory Distributed Active Archive Center) (https://doi.org/10.3334/ORNLDAAC/1007)

Vicente-Serrano S, McVicar T, Miralles D, Yang Y and Tomas-Burguera M 2020 Unraveling the influence of atmospheric evaporative demand on drought and its response to climate change *Wiley Interdiscip. Rev.- Clim. Change* **11** e632

Vishwakarma B D 2020 Monitoring droughts From GRACE *Front. Environ. Sci.* **8** 274

Vishwakarma B D, Devaraju B and Sneeuw N 2018 What is the spatial resolution of GRACE satellite products for hydrology? *Remote Sens.* **10** 852

von Randow C *et al* 2004 Comparative measurements and seasonal variations in energy and carbon exchange over forest and pasture in Ssouth West Amazonia *Theor. Appl. Climatol.* **78** 5–26

Wang D, Morton D, Masek J, Wu A, Nagol J, Xiong X, Levy R, Vermote E and Wolfe R 2012 Impact of sensor degradation on the modis NDVI time series *Remote Sens. Environ.* **119** 55–61

Watkins M M, Wiese D N, Yuan D-N, Boening C and Landerer F W 2015 Improved methods for observing earth's time variable mass distribution with grace using spherical cap mascons *J. Geophys. Res.* **120** 2648–71

Wei J, Cui Y and Luo Y 2023 Rice growth period detection and paddy field evapotranspiration estimation based on an improved SEBAL model: considering the applicable conditions of the advection equation *Agric. Water Manage.* **278** 108141

Werth D and Avissar R 2004 The regional evapotranspiration of the amazon *J. Hydrometeorol.* **5** 100–9

Wrzesien M, Pavelsky T, Durand M, Dozier J and Lundquist J 2019 Characterizing biases in mountain snow accumulation from global data sets *Water Resour. Res.* **55** 9873–91

Wu J *et al* 2016 Leaf development and demography explain photosynthetic seasonality in Amazon evergreen forests *Science* **351** 972–6

Xiong J *et al* 2023 ET-WB: water balance-based estimations of terrestrial evaporation over global land and major global basins *Earth Syst. Sci. Data Discuss.* **2023** 1–47

Yan K, Park T, Yan G, Liu Z, Yang B, Chen C, Nemani R, Knyazikhin Y and Myneni R 2016 Evaluation of modis LAI/FPAR product collection 6. Part 2: validation and intercomparison *Remote Sens.* **8** 460

Zeng Z, Piao S, Lin X, Yin G, Peng S, Ciais P and Myneni R B 2012 Global evapotranspiration over the past three decades: estimation based on the water balance equation combined with empirical models *Environ. Res. Lett.* **7** 014026

Zeng Z, Wang T, Zhou F, Ciais P, Mao J, Shi X and Piao S 2014 A worldwide analysis of spatiotemporal changes in water balance-based evapotranspiration from 1982 to 2009 *J. Geophys. Res.* **119** 1186–202

Zhang K, Kimball J, Nemani R and Running S 2010 A continuous satellite derived global record of land surface evapotranspiration from 1983 to 2006 *Water Resour. Res.* **46** 9

Zhang Y *et al* 2016 Multi-decadal trends in global terrestrial evapotranspiration and its components *Sci. Rep.* **6** 19124

Zhu W, Tian S, Wei J, Jia S and Song Z 2022 Multi-scale evaluation of global evapotranspiration products derived from remote sensing images: accuracy and uncertainty *J. Hydrol.* **611** 127982